Geophys. J. Int. (2009) **178,** 775–791 doi: 10.1111/j.1365-246X.2009.04170.x

High-resolution seismic imaging of the western Hellenic subduction zone using teleseismic scattered waves

J. Suckale,[1] S. Rondenay,[1] M. Sachpazi,[2] M. Charalampakis,[2] A. Hosa[1] and L. H. Royden[1]

[1]*Department of Earth, Atmospheric, and Planetary Sciences, Massachusetts Institute of Technology, Cambridge, MA, USA. E-mail: suckale@mit.edu*
[2]*Geodynamic Institute, National Observatory of Athens,* 118 10 *Athens, Greece*

Accepted 2009 February 26. Received 2009 February 18; in original form 2008 December 3

SUMMARY

The active Hellenic subduction system has long been considered an ideal setting for studying subduction dynamics because it is easily accessible and of limited spatial extent. It has been the focus of numerous seismological studies over the last few decades but, nonetheless, the detailed structure of both the slab and the surrounding mantle remain poorly constrained in an intermediate depth range from 30 to 150 km. The objective of this paper is to fill this gap. The intermediate depth regime is of particular interest because it is pivotal for improving our understanding of the dynamic interaction between subducting lithosphere and the surrounding mantle. An interdisciplinary effort aimed at addressing this challenge is currently undertaken by the 'Multidisciplinary Experiments for Dynamic Understanding of Subduction under the Aegean Sea' (MEDUSA) project. As part of the MEDUSA initiative, a temporary array consisting of 40 densely spaced broad-band seismometers from the IRIS-PASSCAL pool has been deployed in southern Greece. We process the teleseismic data recorded by this array with a migration algorithm based on the generalized radon transform to obtain high-resolution images of the subduction zone in 2-D. The images reveal a sharp Mohorovičić discontinuity (Moho) at depths ranging from 30 km beneath the western margin of the Aegean Sea to 40 km beneath the central Peloponnesus, where it outlines the crustal root of the Hellenides. To the west of the Hellenides, the continental Moho is not identified, but we interpret a pronounced discontinuity imaged at ~20 km depth as the contact between low-velocity sediments and high-velocity crystalline basement. The images also show the subducted oceanic crust as a low-velocity layer that plunges at a constant angle of 21° from west to east. The oceanic crust exhibits low velocities to at least 90 km depth, indicating that the bulk of fluid transfer from the subducted slab into the mantle wedge occurs below this depth. A detailed comparison of images constructed for distinct backazimuthal illuminations reveals deviations in the geometry of the subducted slab. These deviations are attributed to structural and/or compositional changes taking place directly to the north of the MEDUSA array, and are consistent with the existence of a slab tear beneath the Central Hellenic Shear Zone.

Key words: Mantle processes; Seismicity and tectonics; Body waves; Subduction zone processes; Europe.

GJI Seismology

1 INTRODUCTION

The active Hellenic subduction system has long been a target for seismological studies because it is easily accessible, rates of subduction are rapid, and the system poses a high seismic risk for large population centres in Greece. Active deformation of the overriding plate and the rate of convergence are well constrained from GPS data and the geological history of the associated thrust belt is extensively documented. Thus, the Hellenic subduction system presents an excellent opportunity for integrating slab geometry and the seismic structure of the upper-plate lithosphere with the space–time history of subduction, and ultimately, with dynamic processes that govern subduction. Pursuing this research agenda is the main objective of the Multidisciplinary Experiments for Dynamic Understanding of Subduction under the Aegean Sea (MEDUSA) project. The present study contributes one piece to the puzzle by imaging lithospheric structure in the western Hellenides.

The shallow structure of the Hellenic subduction zone above 50 km depth is best known from various reflection and refraction studies (Hirn *et al.* 1996; Mascle & Chaumillon 1998; Clément *et al.* 2000; Bohnhoff *et al.* 2001; Kopf *et al.* 2003; Kokinou *et al.* 2003, 2005). At greater depths, global P-wave tomography shows that the

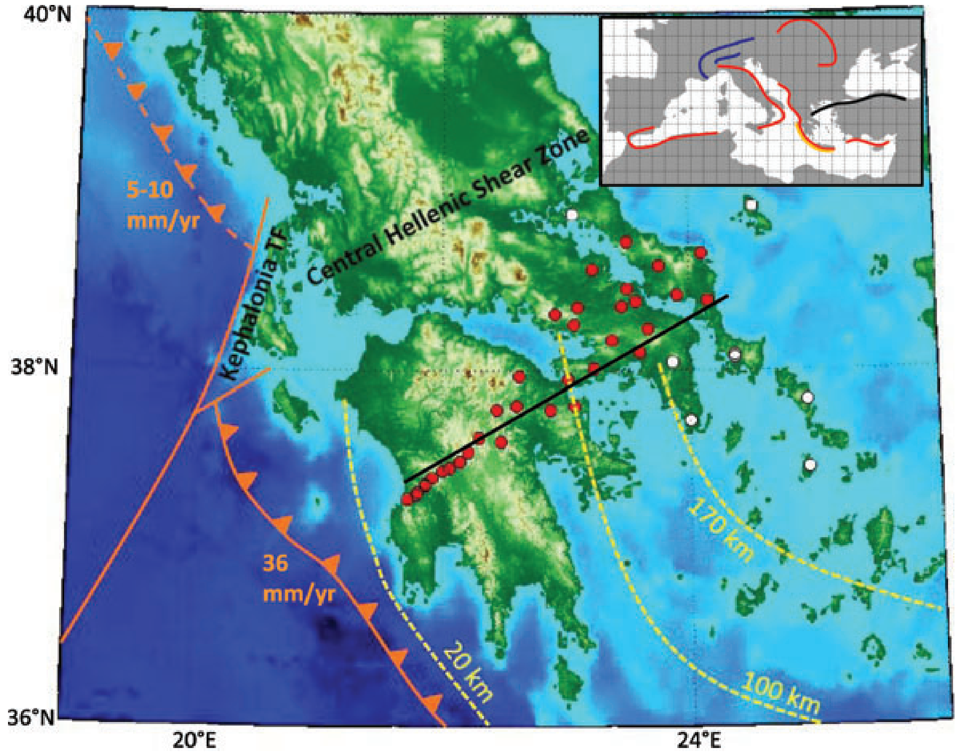

Figure 1. Location of the temporary MEDUSA seismic array. Broad-band seismic stations are represented by circles. The 35 stations that were used in this study are highlighted in red, and the projection line for the 2-D-GRT inversion is indicated in black. Stations in white were discarded in the present analysis, either because of high noise levels or large lateral offsets to the projection line. The yellow dashed lines delineate the depth of the slab inferred from Wadati–Benioff seismicity. The convergence rates are indicated in orange fonts and major tectonic features of the area are named. The inset modified after Royden (1993) shows the location of the study area relative to the Mediterranean region and an overview over the major tectonic features: the North Anatolian fault (black), the collisional mountain belt of the Alps (blue), inactive/slow subduction in the Betics Rif, Carpathians, Apennines and Hellenic arc (red), and active/rapid subduction in the Hellenic arc (red and yellow).

Hellenic subduction zone coincides with high seismic velocities that extend through the upper mantle and transition zone into the lower mantle (Ligdas *et al.* 1990; Spakman *et al.* 1993; Papazachos & Nolet 1997; Piromallo & Morelli 2003; Schmid *et al.* 2006). However, within the intermediate depth range from 30 to 150 km, the detailed structure of the slab and the surrounding mantle remain poorly constrained as compared to other, well-studied subduction systems (e.g. Rondenay *et al.* 2001; Ferris *et al.* 2003; Schurr *et al.* 2003; Zhang *et al.* 2004; Rossi *et al.* 2006). The present study aims at revealing new structural details of the western Hellenic subduction system over this intermediate depth range based on data obtained from a local array of 40 broad-band seismometers deployed for a period of 18 months (Fig. 1).

We employ a recently developed high-resolution seismic imaging technique, the 2-D-generalized radon transform (GRT) inversion (Bostock *et al.* 2001; Shragge *et al.* 2001; Rondenay *et al.* 2001), which inverts the scattered wavefield in the teleseismic *P*-coda to resolve rapid transitions in material properties. Given a sufficiently close station spacing (1.8–18 km Rondenay *et al.* 2005) and good illumination from global teleseismic events, this approach is expected to resolve fine structure with a volume resolution as low as 3–5 km.

2 TECTONIC AND GEOLOGICAL SETTING

The Hellenic thrust belt is located in the east-central Mediterranean region between the slowly converging African and Eurasian plates. It extends over a length of approximately 1000 km from the southern Mediterranean northward through the Ionian Sea to the southeastern Adriatic Sea. Currently, rapid subduction occurs along an arcuate belt extending approximately 400 km from the island of Crete northward to the island of Kephalonia. The slab exhibits a Wadati–Benioff zone dipping $\sim 30^{\circ}$ from 20 to 100 km depth and $\sim 45^{\circ}$ from 100 to 150 km depth (Papazachos *et al.* 2000). The rate of convergence across this part of the Hellenic system is ~ 40 mm yr^{-1} (Clarke *et al.* 1998; McClusky *et al.* 2000) and a well-delineated trench with a maximum water depth of ~ 5 km marks the surface expression of the subduction boundary.

The crust beneath the Ionian Sea, which is currently entering the trench, consists of ~ 6 km of sediments overlying ~ 8 km of crystalline crust. In the accretionary prism, the sedimentary package thickens to up to 10 km (Finetti *et al.* 1991; Hirn *et al.* 1996; Mascle & Chaumillon 1998; Bohnhoff *et al.* 2001; Kopf *et al.* 2003; Kokinou *et al.* 2003, 2005). Together with the modern water depths of 3–4 km in the Ionian Sea, this strongly suggests that the Ionian lithosphere is oceanic in character. The age of the sediments overlying the Ionian lithosphere (Kokinou *et al.* 2003, 2005) indicate that the basement is at least as old as Jurassic and, because rifting in this part of the Mediterranean region occurred in Jurassic and in Triassic time, the most likely age of the Ionian lithosphere is $\sim 200 \pm 50$ Myr. Gravity anomalies point to a very dense, negatively buoyant slab is present within the upper 100–200 km of the subduction system, consistent with subduction of an old oceanic lithosphere (Royden 1993; Tsokas & Hansen 1997).

Active subduction along the Hellenides is attested to by a chain of Pliocene–Quaternary arc volcanoes located ~ 200 km north and east of the present-day Hellenic trench (Fytikas *et al.* 1976, 1984). Based on geochronological dating of the oldest volcanic rock, Le Pichon & Angelier (1979) estimated that the subduction in its present form began about 13 Myr ago. However, the geology of the thrust belt indicates that subduction began in Jurassic time. Over this time period, a succession of oceanic basins and continental shelf/margin domains have been subducted, as reconstructed from the sedimentary rocks and ophiolitic sequences preserved in the thrust belt (e.g. Jacobshagen *et al.* 1978; Papanikolaou 1993; Kopf *et al.* 2003; Papanikolaou *et al.* 2004). In particular, closure of the Pindos ocean occurred in Late Eocene time, followed by subduction of continental to transitional sequences. The initial entry of Ionian oceanic lithosphere into the trench is not well dated, but is probably Middle or Late Miocene in age. Hence the shallow portion of the subducting slab is probably composed of oceanic lithosphere that is approximately 200 Myr old.

Like other subduction systems in the Mediterranean, the Hellenic system is of limited areal extent and the rate and direction of subduction can change along the arc, especially near the ends of the system. The rapidly subducting portion of the Hellenic system, which ends northward at the island of Kephalonia (Fig. 1), is bordered by a zone of slower convergence and subduction that continues northward for 500 km into the central Adriatic region. Here, transitional continental lithosphere is entering the subduction system at GPS-determined rates of 5–10 mm yr^{-1} (Clarke *et al.* 1998; McClusky *et al.* 2000). There is an apparent offset in the subduction boundary between the rapidly and slowly subducting slab segments, across the dextral Kephalonia transform fault (Dewey & Sengör 1979; Finetti 1982; Kahle *et al.* 1993; Peter *et al.* 1998). This fault system broadens as it enters the upper plate lithosphere to comprise a broad zone of transtensional deformation, called the Central Hellenic Shear Zone (CHSZ), with a GPS-determined displacement rate of $\sim$25 mm yr^{-1} (Clarke *et al.* 1998; McClusky *et al.* 2000). The rapidly extending Corinth rift lies within this zone of active extension.

Fig. 2 gives an overview of the GPS data for the study area with respect to Eurasia and highlights that deformation in the Aegean region is dominated by two effects: (1) the westward motion of Turkey and (2) the southwestward motion of the southern Aegean (Le Pichon & Angelier 1981, 1979; McKenzie 1978, 1972, 1970). As first noted by McKenzie (1972), the westward motion of Turkey is likely a result of the continental collision of Arabia and Eurasia in the eastern part of Turkey. However, this escape tectonics cannot explain the southward velocity component of the Aegean block and the significant north–south extension in the Aegean. The driving force for this southward component of motion is thought to be the pull that the downgoing slab in the Hellenic Trench exerts on the Aegean Sea.

The MEDUSA project aims at clarifying the role of roll-back subduction in the evolution of the Hellenic system. One hypothetical reconstruction of the geodynamic evolution of the Hellenic subduction zone is sketched out in Fig. 3: Starting in the Jurassic, continental lithosphere was subducting at a more or less constant rate in both today's northern and southern segment (Fig. 1). Eventually, continental lithosphere was exhausted to the south and followed by denser oceanic lithosphere, which now drives rapid roll-back subduction. The associated trench roll-back and differential subduction rates produced the $\sim$100 km of dextral offset along the Kephalonia Transform and segmented the subducting slab. The possibility of slab segmentation is of note for our study because seismic rays propagating into our array from the northeast may pass through the extending upper plate lithosphere of the CHSZ and/or sample the 3-D structure produced by slab segmentation. The extent to which the slab may be segmented or warped into a lateral ramp geometry is not clear at the present time, but significant 3-D structure in the

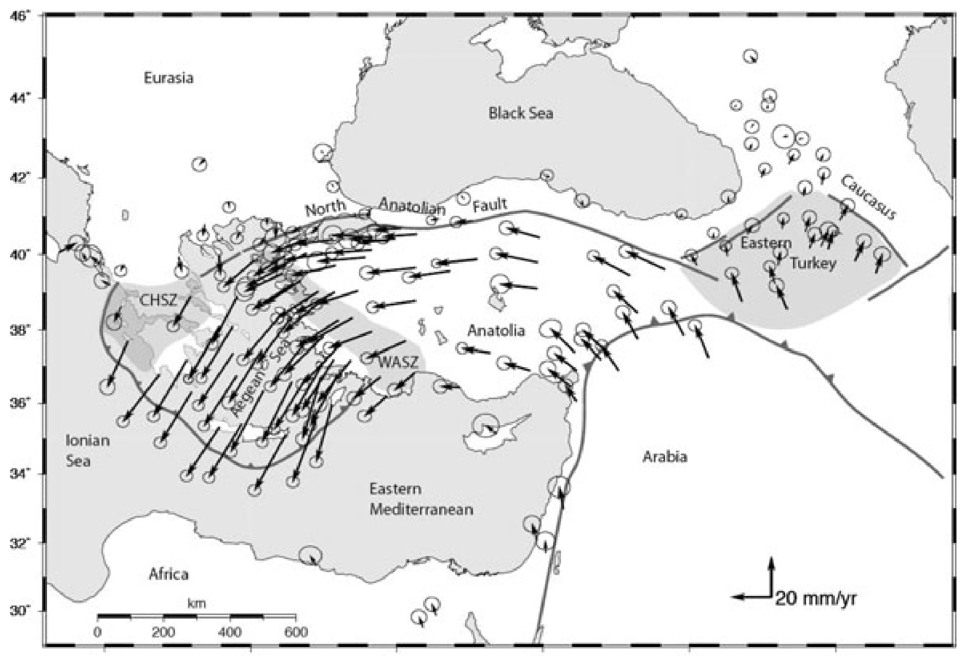

Figure 2. GPS velocities of the Aegean region and Turkey with respect to Eurasia, from McClusky *et al.* (2000). Dark grey lines indicate boundaries between rigid lithospheric fragments. Areas where the motion between fragments is accommodated by regional deformation are shaded in light grey. The Aegean block, which comprises most of the Aegean Sea, the southern part of the Peloponnesus, Crete, and westernmost Turkey, moves as a rigid block. It is bordered by the Central Hellenic Shear Zone (CHSZ) to the northwest and by the Western Anatolian Shear Zone (WASZ) to the northeast. The Hellenic thrust belt marks the limits of the Aegean block to the southwest and to the southeast. Compared to the westward movement of Anatolia, the Aegean block has a more pronounced south-oriented velocity component.

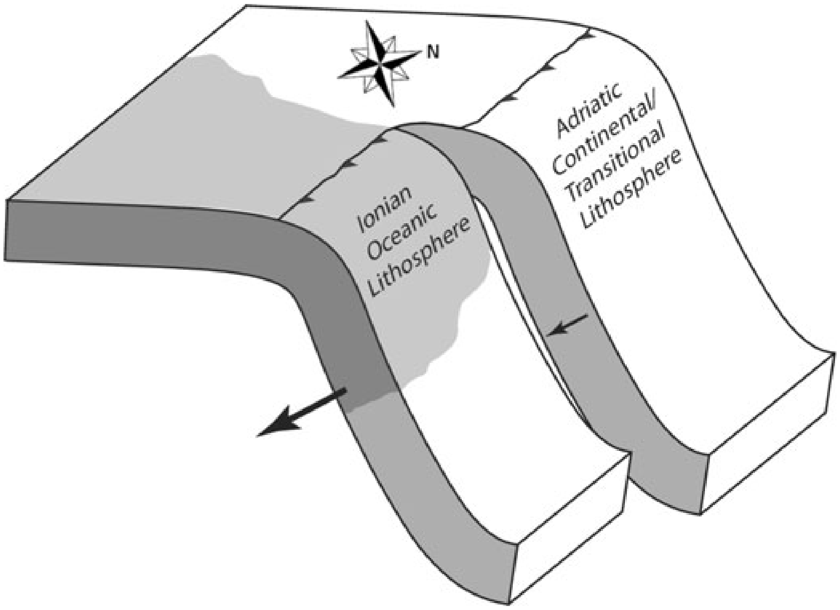

Figure 3. Schematic diagram showing the hypothesized geometry of a segmented slab in the Hellenic subduction zone. In this model, denser oceanic lithosphere to the south began subducting 4–8 Myr ago and now drives roll-back subduction, leading to a dextral offset of approximately 100 km between the slab subducting in the north (northern segment) and the slab subducting in the south (southern segment). The approximate extent of the denser oceanic lithosphere is indicated in grey. Arrows highlight the roll-back velocity in the two segments. Geographic north is highlighted by the compass rose.

slab is probable across this zone. This has implications for the temperature and/or fluid composition of the materials sampled by the seismic waves that traverse this region, and is a point that we shall return to in the discussion section of this paper.

2.1 Previous seismological studies

A variety of previous seismic studies have been undertaken to image the Hellenic subduction zone. These include traveltime tomography (Ligdas *et al.* 1990; Spakman *et al.* 1993; Papazachos & Nolet 1997; Piromallo & Morelli 2003; Schmid *et al.* 2006), marine reflection and refraction profiles (Hirn *et al.* 1996; Mascle & Chaumillon 1998; Clément *et al.* 2000; Bohnhoff *et al.* 2001; Kopf *et al.* 2003; Kokinou *et al.* 2003, 2005) receiver-function analyses (Saunders *et al.* 1998; Knapmeyer & Harjes 2000; Tiberi *et al.* 2001; Li *et al.* 2003; van der Meijde *et al.* 2003; Meier *et al.* 2004; Kreemer *et al.* 2004; Endrun *et al.* 2005; Sodoudi *et al.* 2006; Zhu *et al.* 2006; Snopek *et al.* 2007; Gesret *et al.* 2009), surface-wave dispersion (Calcagnile *et al.* 1982; Mart nez *et al.* 2001; Pasyanos & Walter 2002; Bourova *et al.* 2005; Karagianni *et al.* 2005; Luccio & Pasyanos 2007; Endrun *et al.* 2008), and seismic anisotropy measurements (Hearn 1999; Schmid *et al.* 2004). Furthermore, several recent efforts have focused on constraining the spatial variations in the depth to the continental Moho in the Gulf of Corinth (Tiberi *et al.* 2000, 2001; Clément *et al.* 2004; Zelt *et al.* 2005), central Greece (Sachpazi *et al.* 2007), and the Aegean region (Marone *et al.* 2003; Tirel *et al.* 2004). Both traveltime tomography and receiver functions indicate that the depth of the continental Moho in the study area ranges from 20 to 45 km (Papazachos & Nolet 1997; Tiberi *et al.* 2001; Marone *et al.* 2003; Clément *et al.* 2004; Zelt *et al.* 2005). Depths in excess of 40 km are found beneath the Hellenides in the Peloponnesus and mainland Greece, and are attributed to isostatic compensation of surface relief (Tiberi *et al.* 2000; Marone *et al.* 2003). Shallower Moho depths are found beneath eastern Greece starting in the eastern Gulf of Corinth, one of the most active areas of continental extension in the world (e.g. Armijo *et al.* 1996). Crustal thinning in the Corinth area has been related to Miocene extension involving crustal-scale boudinage (Martinod & Davy 1992; Armijo *et al.* 1996), which resulted in periodic crustal thinning. Then, the Corinth Rift was reactivated about 1 Myr ago and began propagating westward (Armijo *et al.* 1996; Clarke *et al.* 1998; Tiberi *et al.* 2000).

The shallow domain of the subduction (0–30 km) is best constrained from marine reflection and refraction profiles. These have shown that the crust beneath the Ionian Sea is likely oceanic in origin with varying sediment thicknesses from 4 to 6 km west of the trench to up to 10 km in the accretionary prism (Hirn *et al.* 1996; Mascle & Chaumillon 1998; Bohnhoff *et al.* 2001; Kopf *et al.* 2003; Kokinou *et al.* 2003). East of the trench, detailed active source studies in the Ionian islands have identified a bright and slightly landward dipping reflector of variable topography at 13 km depth which is interpreted as the interplate boundary of the subduction zone (Hirn *et al.* 1996; Clément *et al.* 2000).

The deep lithospheric structure (>100 km) of the western Hellenides is known from global (Ligdas *et al.* 1990; Spakman *et al.* 1993; Karason 2002; Piromallo & Morelli 2003) and local (Papazachos & Nolet 1997; Tiberi *et al.* 2000) traveltime tomography. These models find a fast wave speed anomaly that dips steeply and extends well below the transition zone at 660 km (van der Hilst *et al.* 1997). There is also evidence for a sudden increase in subduction angle between 70 and 90 km depth beneath the Gulf of Corinth (Papazachos & Nolet 1997; Tiberi *et al.* 2000). The distribution of earthquake hypocentres outlines a diffuse Wadati–Benioff zone which also exhibits a kink, albeit somewhat deeper at 90–100 km (Papazachos & Nolet 1997).

Traveltime tomography further revealed a lateral discontinuity in the subducted slab on vertical sections cutting through the CHSZ (Fig. 10; Hosa 2008). This observation has been interpreted as evidence for slab detachment in this area (Spakman *et al.* 1988; Carminati *et al.* 1998; Wortel & Spakman 2000), which is of particular interest to this study since a tear in the slab may cause discernible structure in the migrated images.

3 DATA ACQUISITION

The data set for the southern line was acquired over a period of 16 months (2006 July–2007 October) using 40 three-component broad-band seismometers provided by IRIS-PASSCAL. The array is oriented perpendicular to the Hellenic trench in a fan-like configuration (Fig. 1). This setup represents a compromise between obtaining high spatial resolution for teleseismic migration and maximizing versatility towards other imaging techniques. In the west where the slab is shallow, a close and linear station spacing is required to minimize spatial aliasing in the migration. As the slab descends into the mantle the imaging target becomes deeper, thus relaxing the spatial aliasing constraints and allowing for a wider station spread that is more amenable to techniques such as traveltime tomography.

The installation of the stations for the southern line is somewhat unconventional: for security reasons all stations were installed in small buildings, mostly churches, instead of being buried in the ground. The buildings were chosen based on their remoteness, integrity of structure, proximity to bedrock, and coupling to the ground. This strategy fulfilled its purpose in that no components were stolen or damaged—not even during the devastating fires in southern Greece in summer 2007—yielding a total data recovery rate of 96 per cent. However, it raised concern about noise levels. Therefore, we performed a detailed noise analysis based on the technique developed by McNamara & Buland (2004). We used the software by McNamara & Boaz (2005) to compute the component- and station-specific probability density functions (PDFs) to quantify the distribution of seismic power spectral density. We observe three main sources of noise: (1) cultural noise characterized by diurnal variations; (2) machine noise and (3) very long period noise probably related to tilting of the building. Generally, the noise levels of the MEDUSA stations tend to be high with respect to the Peterson noise model (Peterson 1993), particularly in the short period range typical of cultural noise and in the very long period range. Fortunately, most of this noise does not overlap with the frequency range of body-wave arrivals and it can thus be filtered out without affecting the resolution of the image. We designed station-specific Butterworth-bandpass filters based on the noise characteristics at each station to minimize the noise and maximize the stability of the deconvolved waveforms. The filters are zero-phase, with average cut-off frequencies at 0.03 and 0.3 Hz. More details regarding the noise analysis and several examples of PDFs obtained for MEDUSA stations are available in the online supplement.

4 METHODOLOGY

We employ a recently developed imaging technique (Bostock *et al.* 2001; Shragge *et al.* 2001; Rondenay *et al.* 2001), which inverts the teleseismic *P*-wave coda for discontinuities in elastic properties. Specifically, we invert for relative perturbations in *P*- ($\Delta\alpha/\alpha$) and *S*-wave velocities ($\Delta\beta/\beta$) within a reference background velocity model described in Table 1. The technique considers both the forward- and the backscattered wavefields generated at discontinuities in a 2-D isotropic medium. The backprojection operator is based on the GRT and its inverse, and thus the method is commonly referred to as 2-D-GRT inversion (Rondenay *et al.* 2005).

Application of the 2-D-GRT inversion implies computing receiver functions at each station of the array, but adopts a more complex formulation of the scattering problem. Receiver-function profiles are constructed by stacking of normalized *P*-to-*S*-conversion records, binning according to common conversion points (CCP), and mapping to depth (e.g. Dueker & Sheehan 1997). Exemplary receiver functions are included in the online supplement. The inverse problem as cast by the 2-D-GRT can be viewed as a weighted diffraction stack over all sources and receivers, which yields an estimate of the scattering potential at a given point in the subsurface, followed by a linear matrix inversion of the scattering potential for velocity perturbations (Rondenay *et al.* 2005). The weights are determined by the analogy between the forward-scattering equation and the Radon transform, first noted by Beylkin (1985) (see also Miller *et al.* 1987; Beylkin & Burridge 1990). The inverse problem is solved for all points in model space to obtain an image of velocity perturbations. For a full theoretical derivation of the 2-D-GRT inversion see Bostock *et al.* (2001).

Table 1. 1-D reference model used in the 2-D-GRT inversion.

Layer	Depth (km)	α (km s^{-1})	β (km s^{-1})	ρ (g cm^{-3})
1	0–40	6.5	3.7	2.8
2	40–300	8.3	4.7	3.2

Table 2. National Observatory of Athens (NOA) reference model used to localize hypocentres.

Layer	Depth (km)	α (km s^{-1})
1	0–4	5.30
2	4–33	6.00
3	33–45	6.88
4	44–85	7.90
4	85–300	8.10

The 2-D-GRT inversion operates on a series of individual forward- and backscattered modes. The contribution of each mode is inverted based on analytical expressions for the traveltimes and amplitudes of the relevant combination of incident and scattered wave (Rondenay *et al.* 2001). In particular, we consider (1) forward scattering of the incident *P*-wave into *S* (abbreviated by *S*), (2) the free-surface-reflected *P*-wave into backscattered *P* (abbreviated by *PP*), (3) the free-surface-reflected *P*-wave into backscattered *S* (abbreviated by *PS*), and finally the free-surface-reflected *S*-wave into, (4) backscattered *Sv* (abbreviated by *SSv*) and (5) backscattered *Sh* (abbreviated by *SSh*). The various scattering modes are weighted based on the rationale developed in Rondenay *et al.* (2001).

The resolving power of the 2-D-GRT inversion has been extensively studied using synthetic and field data (Bostock *et al.* 2001; Shragge *et al.* 2001; Rondenay *et al.* 2005, 2008), and has been shown to depend largely on the frequency content of the scattered signal and on the source distribution. The maximum volume resolution is approximately equivalent to a quarter of the wavelength of the scattered signal (for backscattered waves). Given the high cut-off frequency of 0.3 Hz used to filter the signal, we therefore expect a maximum volume resolution of the order of 3–4 km for structure in the lower crust and upper mantle.

Rondenay *et al.* (2005) demonstrated that the robustness of the image obtained through the 2-D-GRT inversion might be compromised if the assumptions inherent to the technique are not met. In our context the two most important assumptions are that (1) the imaged lithospheric structure is 2-D and (2) that material properties are isotropic. We note that both the Hellenic slab (Karason 2002) and the continental Moho in the Aegean region (Makris 1978; Papazachos & Nolet 1997; Tiberi *et al.* 2000; Marone *et al.* 2003)

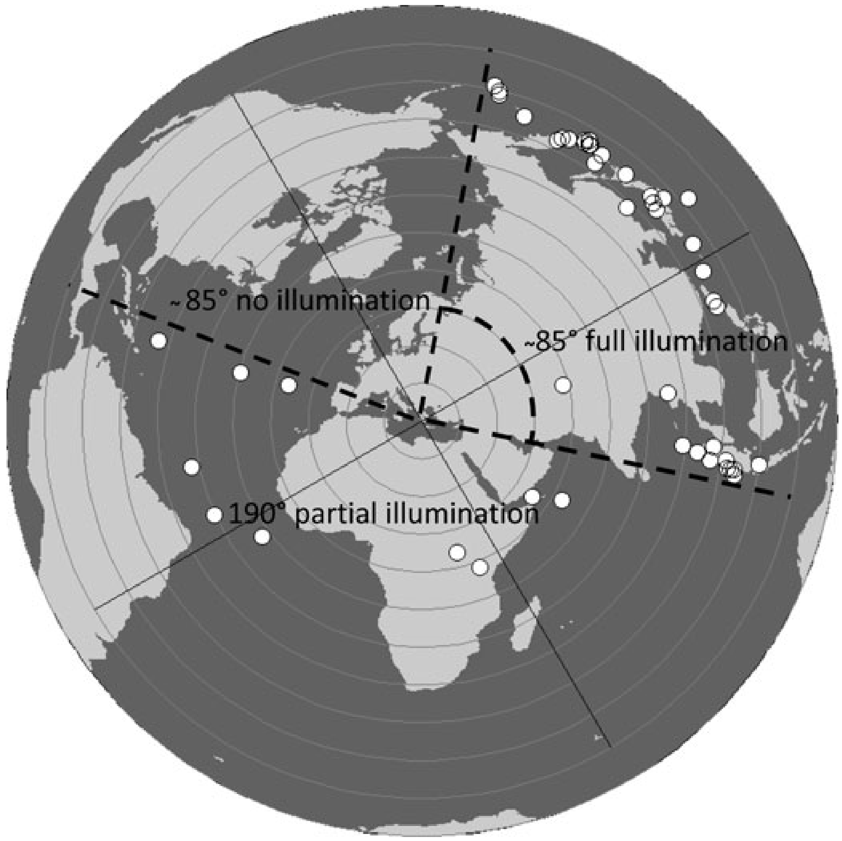

Figure 4. Spatial distribution of the 48 events (white dots) included in the composite image. The grey concentric circles denote 10° epicentral-distance increments. Note that all events fall within the 30°–90° epicentral distance range. The quality of illumination of the study area as a function of backazimuth is indicated. Due to abundant natural seismicity in the Asian Circum-Pacific region, optimal illumination is achieved for a ∼ 85° backazimuthal range starting from the Aleutian islands in the northeast to Indonesia in the southeast. Events from central Africa and the mid-ocean ridge yield another 190° of partial illumination.

may not strictly fulfil the assumption of two dimensionality. Furthermore, seismic anisotropy has been documented throughout the Aegean region (Hearn 1999; Schmid *et al.* 2004). We will pay particular attention to these issues when analysing the images.

5 DATA SELECTION

In order to ensure maximum resolution, the lithospheric structure to be imaged through 2-D-GRT inversion should be illuminated by teleseismic waves arriving from all backazimuthal directions. This comprehensive backazimuthal illumination is an ideal not generally achieved in practice, because of the spatially heterogeneous distribution of natural seismicity. In the case of Greece, event coverage can be broken into three distinct ranges: comprehensive illumination is achieved for an backazimuthal range of ∼85°, between approximately 12 and 98° backazimuths; partial illumination is available for an additional 190° (roughly 98–284° backazimuths); and there is no coverage in a window of ∼85°, between approximately 284–12° (Fig. 4).

Not all earthquakes produce seismic data that is amenable to 2-D-GRT inversion. Accordingly, we selected events for analysis if they fulfilled the following criteria (Rondenay *et al.* 2005, 2001): (1) 30°–90° epicentral distance from the centre of the array, to avoid phases triplicated in the mantle transition zones or diffracted at the core-mantle boundary, (2) pronounced first *P*-arrival observed on both vertical and radial components, (3) a brief source wavelet, that is, shorter than 50 s, (4) a sufficiently high magnitude (larger >5.5 mb) and (5) no overlaps with pre- or aftershocks. A large number of events in the 12–98° backazimuthal range meet these criteria. This allows us to narrow down the selection in this range by requiring coherence among images from individual scattering modes, and coherence among the composite (i.e. combined-modes) images of neighbouring events. This additional step eliminates traces that are unstable due to source effects. Limited event coverage at other backazimuths prevents the application of this additional selection criterium and we therefore include all events and phases that produce a stable image in this range. The epicentres of the 48 events included in the composite image are shown in Fig. 4.

6 RESULTS

In this section, we present the results from 2-D-GRT inversion applied to the MEDUSA data. We first discuss the images produced through simultaneous inversion of the entire data set. Then we investigate backazimuthal contributions to the image in order to address the possible effects of anisotropy and departure from 2-D geometry.

6.1 Composite images

The composite images showing the subsurface structure of the southern Hellenic subduction zone are given in Fig. 5. They are computed for a N60°E azimuth. The geographic location of the projection line is also displayed in Fig. 1. The images are based

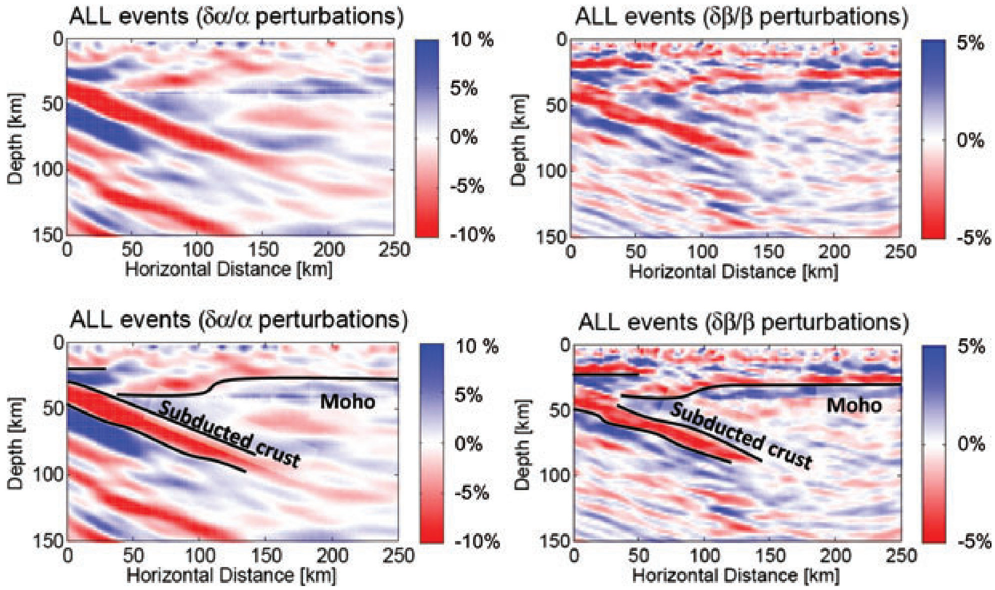

Figure 5. Composite images obtained through 2-D-GRT inversion for 48-high quality events (see Fig. 4 and Table 6 for details). All images were computed based on a 60° projection angle with respect to north shown on Fig. 1. The left images show perturbations in *P*-wave velocity $\delta\alpha/\alpha$ and the images on the right show perturbations in *S*-wave velocity $\delta\beta/\beta$. The colour shading indicates the magnitude of the velocity perturbations in per cent (see colour bar for scale), with blue and red representing fast and slow velocity perturbations, respectively. The top panels show only the raw images, while the bottom panels additionally contain our structural interpretations.

on the simultaneous inversion of the 48 selected events (Fig. 4) and phases detailed in Table 6. The two images show perturbations to the *P*-wave velocity $\delta\alpha/\alpha$ (left figures) and to the *S*-wave velocity $\delta\beta/\beta$ (right figures). These perturbations are represented as rapid variations in relative velocities (red-to-blue or blue-to-red), where red and blue shadings denote slow and fast relative velocities, respectively. Note that the colour scale varies for the *P*-(±10 per cent) and *S*-velocity perturbations (±5 per cent).

Both images are consistent in terms of the lithospheric structure they reveal. This consistency suggests that the images are robust since they are based on different scattered phases and thus provide essentially independent pieces of information. Generally, the *S*-wave image is more rich in structural detail—as should be expected because three backscattered phases (*PS*, *SSv* and *SSh*) contribute to it. In comparison, only one phase (PP) contributes to the *P*-wave image. Based on the images presented in Fig. 5, we identify two prominent lithospheric features in the western Hellenides. First, a sharp positive (downward slow-to-fast) velocity contrast reminiscent of the Moho is observed across most of the array in the 23–40 km depth range. The discontinuity reaches its maximum depth of 40 km roughly in the centre of the study area (∼50–90 km from its western margin), and rises rapidly in ENE direction to attain a stable depth of ∼30 km in the eastern portion of the profile. The continuation of this discontinuity to the WSW portion of the profile is less clear: after a seemingly discontinuous step, a similarly sharp positive velocity contrast appears at a constant depth of ∼23 km. However, as discussed in more detail in Section 7.2, we argue that this discontinuity does not represent the Moho. Second, there is a clearly defined low-velocity layer that dips from WSW to ENE at a constant angle of ∼21°. It is observed across most of the profile down to a depth of 90 km in the *S*-wave image and deeper in the *P*-wave image (Fig. 5). Based on a comparison with the local Wadati–Benioff zone (Papazachos *et al.* 2000; Christova 1992) and the analogy to images of other subduction zones imaged with the same method (e.g. Rondenay *et al.* 2008), the low velocity may be attributed at least in part to the hydrated crust of the Hellenic slab. However, we note that this layer appears unusually thick (15–22 km) for oceanic crust. Resolution tests detailed in the online supplement reveal that this thickness is a robust observation rather than an artefact caused by the use of an inappropriate projection angle for the 2-D profile. Possible explanations for this feature are discussed in Section 7.

6.2 Backazimuthal contributions

We investigate backazimuthal contributions to the seismic image by constructing profiles using incident waves that originate in restricted backazimuthal ranges (Figs 6–8 and Table 3). The backazimuthal bins are chosen such that they provide a quasi-regular backazimuthal sampling and take into account clusters of seismicity in the Pacific and in Africa. This procedure results in six bins that are spaced evenly at 20°–25° (see Table 3): (1) Aleutian islands, (2) Kuril islands, (3) Central Japan, (4) Taiwan, (5) Indonesia and (6) Somalia. When comparing profiles created by individual events within each bin, we find excellent coherence between single-mode (*S*, *PS*, *PP*, *SSv* and *SSh*) and combined-mode images. This result is expected based on our event selection criteria. Two examples illustrating the expected coherence within a specific backazimuthal bin are given in the online supplement.

For the comparison of the various backazimuthal contributions, we construct each bin-dependent image using the same number of events to avoid biases in signal-to-noise ratio between regions of variable event coverage. We use two events per bin (see Table 3), as this is the maximum number of events available for bin 6. Profiles are computed for each scattering mode and are presented in Figs 6–8. We limit our discussion to the deviations between the *S*-, *PP*- and *SSh*-modes as they afford maximum scattering from the slab for obliquely incident ray from NE and SE backazimuths (Rondenay *et al.* 2001). The corresponding comparisons of backazimuthal contributions for the *PS*- and *SSv*-phase are included in the online supplement. We note that the images constructed with only the *S*-mode are generally more diffuse, because forward-scattered

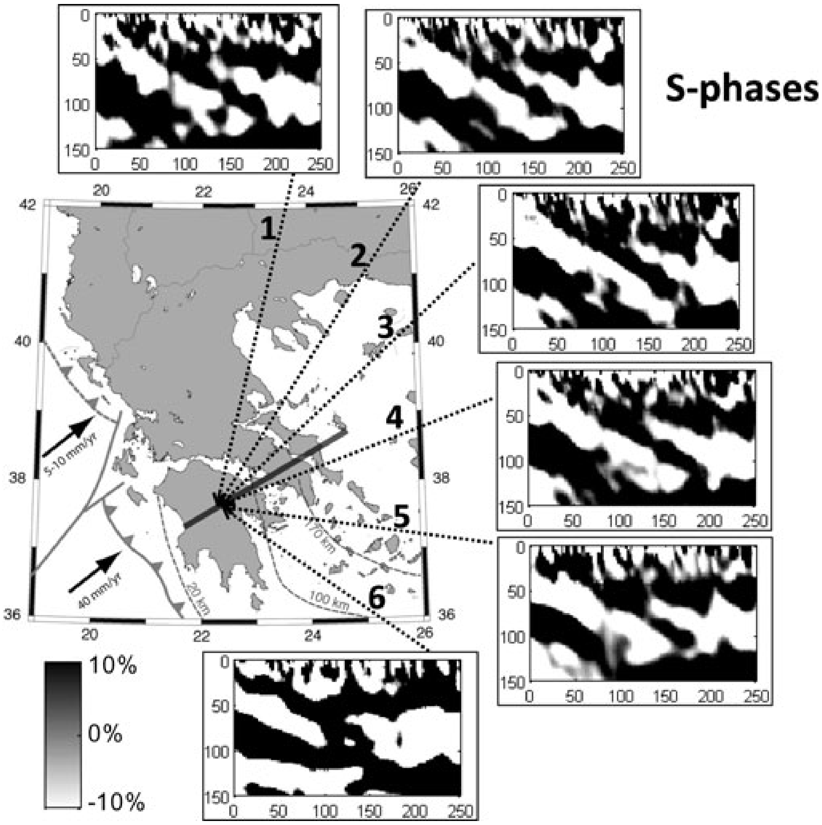

Figure 6. Backazimuthal variations for the *S*-mode images. We compare how the *S*-mode images vary as a function of the backazimuth of the incident teleseismic waves. Each image is created using two high quality events originating within a narrow backazimuthal range ($\sim$20°) centred on the numbered lines. Starting from the northernmost backazimuths, the bins correspond to events located in the following regions: (1) the Aleutian Islands, (2) Kuril Islands, (3) Central Japan, (4) Taiwan, (5) Indonesia and (6) offshore Somalia. We observe that images in bins 1–4 are consistent in terms of slab dip and slab thickness. Images in bins 5 and 6, on the other hand, show a more shallowly dipping slab. For details on the included events and scattering modes see Table 3. A coloured version of this figure is available in the online supplement.

modes provide lower resolution than backscattered ones (Section 6.1). However, as in previous applications of the 2-D-GRT inversion to subduction zone imaging (Rondenay *et al.* 2001, 2008), we expect forward and backscattered modes to retrieve coherent geometrical attributes at least for the subduction interface.

The comparison of the different backazimuthal contributions reveals some interesting deviations. We find that the outline of the dipping low-velocity layer is generally coherent across all backazimuths for *PP*- and *SSh*-modes (Figs 7 and 8), despite the lower quality *PP*-image in bin 6 and contamination by multiples in all *SSh*-mode images. Conversely, the *S*-mode profiles (Fig. 6) show variations in slab dip ranging from high angle ($\sim$34°) for regions 1–4, to an intermediate angle ($\sim$26°) in region 5, to a shallow angle ($\sim$21°) approaching that observed in other modes in region 6. We also note variations in the depth extent of the dipping low-velocity layer from one backazimuthal bin to another. However this may not be a robust feature due to loss of resolution near the edge of the model, an effect that is exacerbated by limited event coverage (Rondenay *et al.* 2005).

Despite the appeal of the comparison done in Figs 6–8, each backazimuthal image is based only on two events and may be dominated by event-specific artefacts. We must therefore verify whether the observed differences in slab dip are robust when more events are included. Two regions lend themselves to such a detailed comparison by virtue of their high level of seismicity: Indonesia and the Kuril Islands. These regions provide illumination from eastern and northern backazimuths, respectively. Fig. 9 shows the single-mode images for the *S*, *PP* and *SSh* phase based on the 10 best events from each region (see Tables 4 and 5 for details on the included events) and supports the initial finding: while the apparent slab dip is $\sim$21° in both *PP*-mode and *SSh*-mode images, the slab dip on the *S*-mode images is much steeper for Kuril Islands events (35°) than for the Indonesian events (26°). These differences are significant: based on the analysis of Ewald scattering spheres (Rondenay *et al.* 2005, 2008), we expect that the dip resolution at the top of the slab is $<$5°, where the low-velocity layer is observed. The variations in slab dip between different modes and backazimuthal bins could be related either to deviations from the assumptions made in 2-D-GRT inversion (two-dimensionality and isotropy), the usage of an inaccurate background velocity model, or to a combination of these factors. We investigate this issue further in the following section.

7 DISCUSSION

In this section, we discuss the tectonic, geological, and geodynamic implications of the seismic images obtained for southern Greece by 2-D-GRT inversion. Specifically, we address the following questions.

(i) What is the nature of the subducted material? Is there evidence for metamorphic changes in the slab with increasing depth and pressure?

(ii) What do the variations in the depth to the continental Moho imply for the deformational regime in the overlying plate?

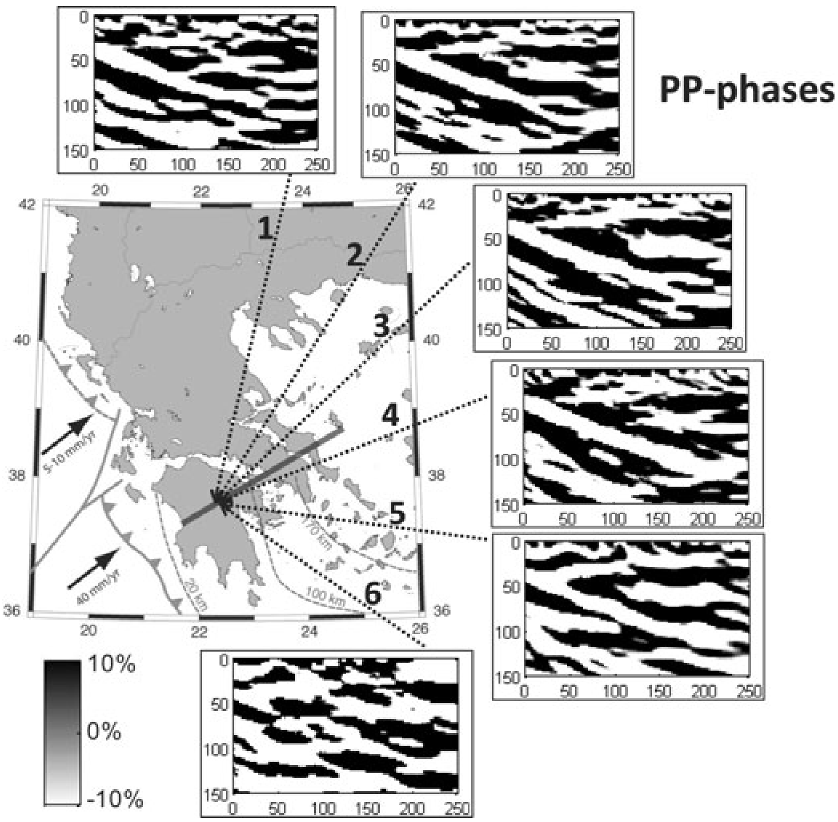

Figure 7. Backazimuthal variations for the *PP*-mode images. The profiles are created using the same events as those used in Fig. 6. We observe that images in bins 1–5 are consistent both in terms of slab dip and slab thickness. In the image from bin 6, the *PP*-scattering response of the slab is weak, which is an effect of non-optimal incidence angle—that is, most of the surface-reflected, downgoing *P*-wave energy is converted into *S* at the slab for this incidence angle. For details on the included events and scattering modes see Table 3. A coloured version of this figure is available in the online supplement.

(iii) What do the backazimuthal variations in the composite image reveal about subduction dynamics in the western Hellenides?

7.1 Subducting slab

As discussed in Section 2, the slab currently subducting beneath the Hellenides south of Kephalonia is thought to be old ($\sim$200 Myr) oceanic lithosphere. But the presumable oceanic nature of the slab is not consistent with a thickness of 15–20 km as may be inferred from the dipping low-velocity layer imaged beneath southern Greece. Consequently, this low velocity layer is perhaps not attributable only to subducted oceanic crust. Based on studies of other subduction zones, there exist at least three possible explanations for the thick layer of low-velocity material subducting below our study area.

First, it could represent a portion of foreland that had a thicker crust than is currently observed in the Ionian Sea region, similar to the exotic doubly thick Yakutat terrain reported in southern Alaska (Rossi *et al.* 2006). Since we observe a low-velocity layer of constant thickness, it follows that the transition from this exotic terrane to the oceanic-type crust reported for the Ionian Sea (Hirn *et al.* 1996; Clément *et al.* 2000; Kokinou *et al.* 2003, 2005) would have to occur just beyond the WNW margin of our profile. However, there is no evidence for a sudden transition between different crustal terrains in the accretionary wedge off the shore of the western Peloponnesus (Finetti *et al.* 1991).

Second, the subducted oceanic crust could be overlain by a thick layer of sediments characterized by low seismic velocities. It seems unlikely that the full thickness of sediments observed in the Ionian Sea foreland (6 km) is present within the subducting slab at subcrustal depth. Arguments against this interpretation include the low density and high buoyancy of the sedimentary package and the fact that the sedimentary wedge in the Ionian Sea is currently shortening and thickening above a basal décollemont zone(s) that extends for several hundred kilometres outboard of the trench (Finetti *et al.* 1991). The existence of basal décollemont zone(s) indicates that most of the sedimentary sequence is moving with the upper plate and that its stratigraphy allows for the development of extensive shear surfaces between the lower part of the sedimentary unit and the underlying basement rocks. Nevertheless, the presence of some low-velocity sediments along the upper surface of the subducting slab can clearly not be ruled out.

Third, a layer of serpentinized mantle peridotite exhibiting low seismic velocity, either directly below the subducted oceanic Moho (Rüpke *et al.* 2004) or above the subduction interface in the mantle wedge (Kawakatsu & Watada 2007), can add to the apparent thickness of the subducted oceanic crust. Although no thermal model is available for the Hellenic subduction system in our study area, general models by Rüpke *et al.* (2004) predict that serpentine would be stable in either domain to depths exceeding 100 km assuming a slab age of $>$120 Myr and a subduction rate of 20–60 mm yr^{-1}.

Based only on our imaging, it is not possible to discriminate between these three models. We also note that the resolution of the composite images (Fig. 5) is reduced with respect to the theoretically expected resolution of 3–5 km (Section 1), because of

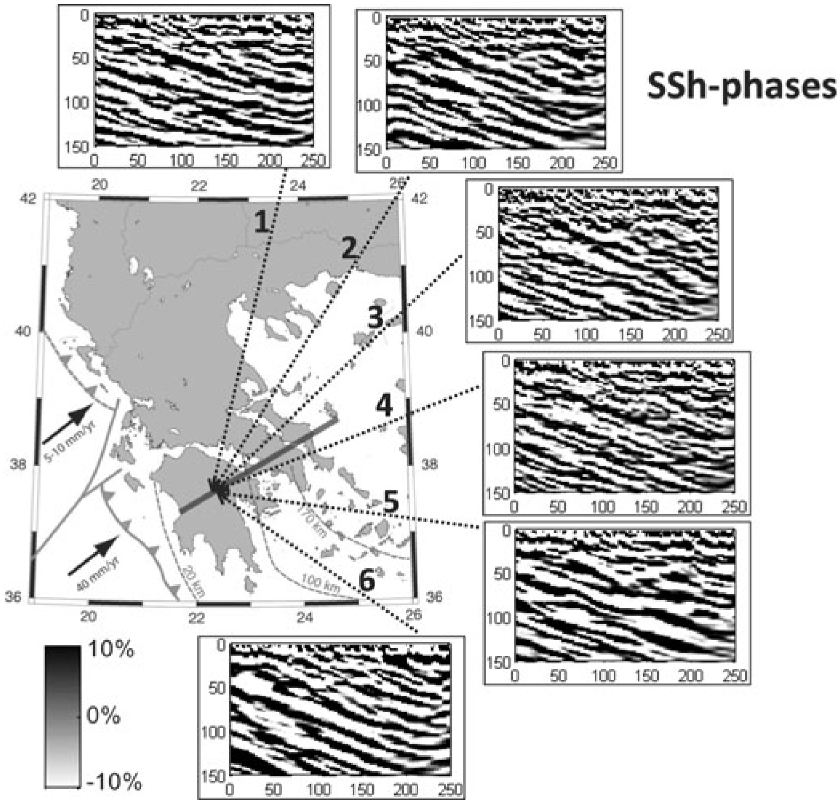

Figure 8. Backazimuthal variations for the *SSh*-mode images. The profiles are created using the same events as those used in Fig. 6. All images contain significant artefacts caused by multiples: they show 'slab-like' low-velocity layers at various depths parallel to the actual location of the slab interface. In the simultaneous inversion of a large number of events these multiples cancel out, but for the images shown here it is difficult to distinguish between signal and artefact. Nevertheless, a dipping low-velocity layer is observed consistently starting at ∼50 km depth in the western edge of all profiles. The highest-quality image stems from bin 6 (Somalia) and indicates the presence of a low velocity layer of approximately constant thickness dipping at ∼21°. There is no apparent variation in dip of the low-velocity layer between the different backazimuths. For details on the included events and scattering modes see Table 3. A coloured version of this figure is available in the online supplement.

Table 3. Events included in the analysis of backazimuthal contributions.

Date	Time	Lat (°N)	Lon (°E)	Depth (km)	mb	*S*	*PP*	*PS*	*SSv*	*SSh*
				Aleutian islands						
2006/7/08	20:40:01	51.21	−179.31	22	6.2	1	1	1	1	1
8/15/07	20:22:11	50.32	−177.55	9	6.3	1	1	1	1	1
				Kuril islands						
2006/9/30	17:50:23	46.35	153.17	11	6.1	1	1	1	1	1
2006/12/7	19:10:22	46.15	154.39	16	6.3	1	1	1	1	1
				Central Japan						
2007/3/25	0:41:58	37.34	136.59	8	6.1	1	1	1	1	1
2007/7/16	1:13:22	37.54	138.45	12	6.5	1	1	1	1	1
				Taiwan						
2006/10/09	10:01:47	20.65	120.02	14	6.0	1	1	1	1	1
2006/12/26	12:26:21	21.80	120.55	10	6.4	1	1	1	1	1
				Indonesia						
2007/8/08	17:04:58	−5.93	107.68	291	6.1	1	1	1	1	1
2007/9/20	8:31:14	−1.99	100.14	30	6.3	1	1	1	1	1
				Offshore Somalia						
2006/12/30	8:30:50	13.31	51.37	15	5.9	0	1	1	1	1
2007/1/17	23:18:50	10.13	58.71	8	5.8	1	0	1	0	1

incomplete illumination (Fig. 4) and backazimuthal inconsistencies (Section 6.2). Future efforts in regional traveltime tomography, single-station receiver-function modelling, careful relocation of intraslab seismicity, and region-specific thermal models will be necessary to further constrain the cause of the unusual thickness of the low-velocity layer.

Regardless of the exact explanation for the thick low-velocity layer, all the proposed models support that the observed

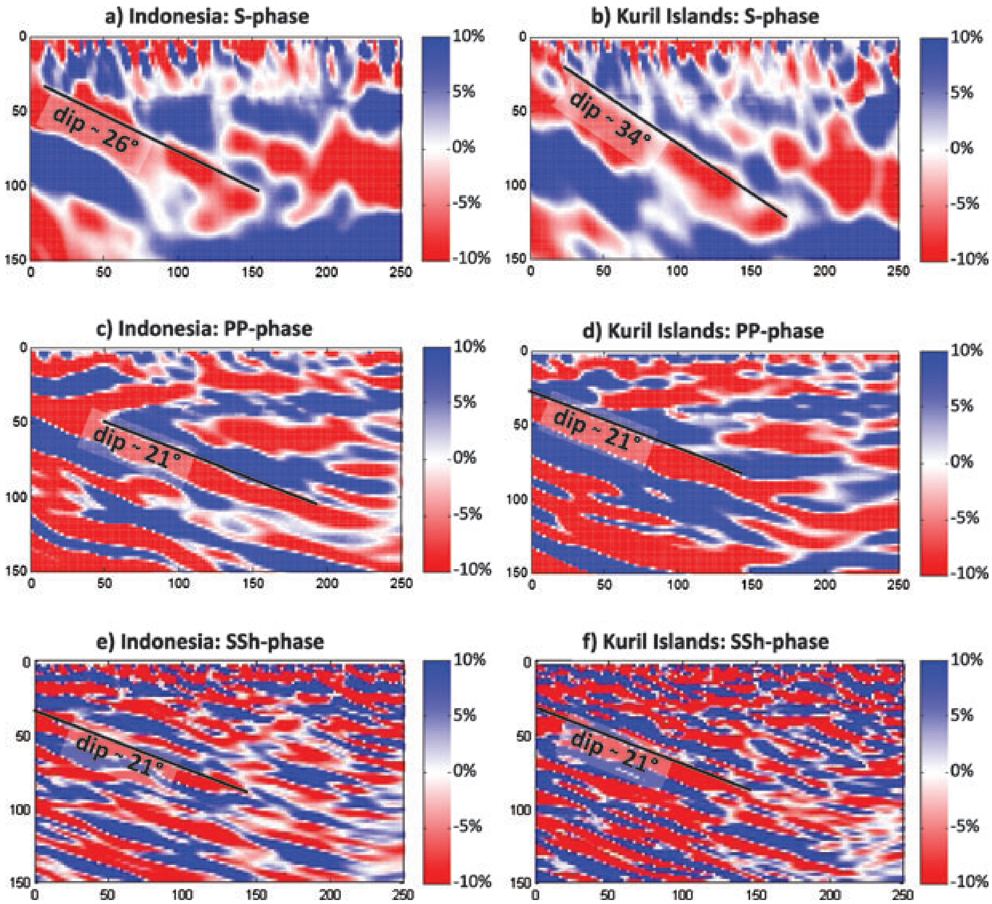

Figure 9. Comparison between images based on events incident from the east (Indonesian sources) and events incident from the north (Kuril Island sources). We compare the *S*-, *PP*- and *SSh*-mode for ten high quality events from Indonesia (panels a, c and e) and from the Kuril islands (panels b, d and f). While all *PP*- and *SSh*-mode images are consistent in terms of slab dip, the *S*-mode images vary significantly as a function of backazimuth. The *S*-mode image based on events from the Kuril islands shows a steep slab of ∼34° dip, whereas the images based on Indonesian events show a slab whose dip (23°) is consistent with the other modes. For details on the included events and scattering modes see Tables 4 and 5.

Table 4. 10 high quality events from the Kuril Islands included in the region-specific image.

Date	Time	Lat (°N)	Lon (°E)	Depth (km)	mb	*S*	*PS*	*PP*	*SSv*	*SSh*
2006/6/22	10:53:12	45.42	149.34	95	6.1	1	1	0	0	1
2006/8/20	3:01:02	49.82	156.42	26	5.8	1	1	1	1	1
2006/8/24	21:50:37	51.15	157.52	43	5.9	1	1	1	1	1
2006/9/30	17:50:23	46.35	153.17	11	6.1	1	1	1	0	1
2006/10/1	9:06:02	46.47	153.24	19	6.1	1	1	0	0	1
2006/11/15	11:14:14	46.59	153.27	10	6.5	1	1	0	1	0
2006/11/15	19:25:25	47.01	154.98	10	5.6	1	1	0	0	1
2006/11/15	21:22:21	47.28	154.15	12	6.0	1	1	1	1	1
2006/12/7	19:10:22	46.15	154.39	16	6.3	1	1	1	1	1
2007/5/30	20:22:13	52.14	157.29	116	6.4	1	1	0	1	1

low-velocities are an indication of water transport into the mantle. Therefore, as for seismic profiles of other subduction zones, a disappearance of the dipping low-velocity layer at depth could be interpreted as marking the region where slab dehydration takes place, whether by eclogitization of the hydrated oceanic crust or by destabilization of serpentinized mantle peridotites (Rondenay *et al.* 2008). In our study area, the low-velocity layer is visible down to 90 and 120 km depth in the $\delta\beta/\beta$ and $\delta\alpha/\alpha$ composite profiles, respectively (Fig. 5), and down to 100–150 km depth in the different backazimuthal contributions from individual scattering modes (Figs 6–8). These deviations in the maximum depth of observation of the low-velocity layer are likely a consequence of either variable dip resolution of the different scattering modes and/or backazimuthal inconsistencies between different scattering modes caused by 3-D structure. Thus, while our results do not allow for a conclusive estimate of the depth range over which slab dehydration takes place, we can infer that the bulk of fluid transfer from the slab to the mantle wedge occurs deeper than 90 km. This range of

Table 5. 10 high quality events from Indonesia included in the region-specific image.

Date	Time	Lat (°N)	Lon (°E)	Depth (km)	mb	*S*	*PP*	*PS*	*SSv*	*SSh*
2006/7/27	11:16:40	1.71	97.15	20	6.1	0	0	0	1	1
2006/12/1	3:58:22	3.39	99.08	204	6.0	1	1	1	1	1
2006/12/17	21:10:22	4.82	95.02	36	5.7	1	1	0	0	0
2007/1/8	12:48:41	8.08	92.44	16	6.3	0	1	1	1	1
2007/3/6	5:49:25	−0.49	100.53	11	5.9	0	1	0	0	1
2007/3/7	10:53:38	1.96	97.91	35	5.7	0	1	0	1	0
2007/8/08	17:04:58	−5.93	107.68	291	6.1	1	1	1	0	1
2007/9/13	16:09:16	−3.16	101.53	49	6.1	1	1	0	0	0
2007/9/14	6:01:32	−4.08	101.17	23	6.3	1	1	0	0	0
2007/9/19	7:27:51	−2.75	100.89	35	5.7	1	1	1	0	1
2007/9/20	8:31:14	−1.99	100.14	30	6.3	1	1	1	1	1

dehydration depths is generally consistent with that predicted by thermal models for the subduction of old oceanic lithosphere (Rüpke *et al.* 2004; Rondenay *et al.* 2008).

7.2 Crustal structure of the overriding plate

We interpret the sharp slow-to-fast discontinuity observed in the central and eastern portions of the image to represent the continental Moho of the overriding plate. Its depth fluctuations are largely consistent with prior results from regional receiver-function studies (Marone *et al.* 2003; Li *et al.* 2003; Sodoudi *et al.* 2006; Zhu *et al.* 2006; Sachpazi *et al.* 2007), and investigations of crustal thickness in the Gulf of Corinth area (Tiberi *et al.* 2000, 2001; Clément *et al.* 2004; Zelt *et al.* 2005). The large variations in Moho depth attest to the complex tectonic evolution of Greece and to the interplay between compressional processes associated to subduction and extension in the backarc basin area: Below the central Peloponnesus, the Moho reaches its maximum depth of 40 km as it outlines the root of the Hellenides. Below the Gulf of Corinth, the Moho shallows rapidly from ∼40 km in the western to ∼30 km in the eastern part of the Gulf reflecting the intense past and present crustal extension in this area (Armijo *et al.* 1996; Clarke *et al.* 1998; Tiberi *et al.* 2000; Zelt *et al.* 2005).

A pronounced discontinuity in seismic velocity can be observed in the western part of our profile at ∼20 km depth. This feature may be interpreted as (1) an anomalously shallow and previously unrecognized Moho beneath the western Hellenides, (2) a doubling of the Moho due to incorporation of a mantle slice into the crust or (3) a strong velocity contrast within the continental crust. The first two options are unlikely because gravity data shows no evidence for a high density mantle layer at shallow depths beneath the western Hellenides (Royden 1993; Tsokas & Hansen 1997). Moreover, in the absence of a suture zone, it is unusual for the Moho to jump discontinuously by ∼20 km in depth as is the case for the prominent discontinuity located at 40 km in the central study area and at ∼23 km depth in the WNW portion of the profile. Therefore, we favour the third option and propose that instead of representing the continental Moho, the discontinuity at ∼23 km in the WNW portion of the study area represents a mid-crustal contact between an upper crust composed of low-velocity sediments and a mid-to-lower crust composed of high-velocity crystalline continental basement.

Geological field observations demonstrate that the upper crust of the Hellenides is composed of an imbricate stack of sediments comprised largely of Mesozoic carbonate rocks (Jacobshagen *et al.* 1978; Brown & Robertson 2003; Neumann & Zacher 2004). The thickness of this stacked sedimentary package is probably more than 12 km, perhaps as much as 15–20 km. Thus the strong velocity contrast imaged beneath the western Hellenides at 20 km depth is approximately consistent with geological estimates of the total thickness of the sedimentary package. These sedimentary rocks and the higher-velocity crystalline crust below are likely to have been stripped from the downgoing slab in Late Eocene to Present time, and incorporated into overriding crust at different structural levels. If the discontinuity at 23 km depth is indeed an intracrustal boundary, then the seismic profiles indicate that the continental Moho is truncated by the slab west of the Hellenides. The interface between the slab and the crust in that region is denoted by a sharp seismic boundary, which may be due to elevated pore-fluid pressure resulting from progressive dehydration of the slab and entrapment of the fluids at the interface (Audet *et al.* 2009).

7.3 Structure of the mantle wedge

The observed backazimuthal variations—an unusually steep slab dip (∼34° instead of ∼21°) apparent only on the *S*-mode image for northern backazimuths—indicate that the lithospheric structure in the southern Hellenides deviates from the assumed 2-D geometry with isotropic material properties embedded in a uniform 1-D background-velocity model. Below, we assess the validity of three key assumptions made in the 2-D-GRT inversion algorithm used in this study, namely that (1) the lithospheric structure is 2-D, (2) material properties are isotropic and (3) the background velocities are known and laterally uniform across the whole model.

First, concerning geometrical constraints on the imaged structure, we note that deviations from the assumed 2-D geometry will affect the resulting image only if they occur within less than 100 km lateral offset from the imaging plane (Rondenay *et al.* 2005). This implies that the arcuate geometry of the Hellenic slab at regional scale (Figs 1 and 2), should not affect the images produced using incident waves from eastern and southern backazimuths, since the curvature of the arc becomes pronounced only at lateral offsets >100 km. Conversely, to the north of the array, there is evidence from traveltime tomography that the Hellenic slab is tearing (Fig. 10; see also Spakman *et al.* 1988; Carminati *et al.* 1998; Wortel & Spakman 2000). Independent of its exact geometry (along-strike as suggested by Wortel & Spakman 2000, or slab perpendicular below the Kephalonia Transform as hypothesized in Fig. 3), a slab tear may cause 3-D structure that extends into the region sampled by incident waves from northern backazimuths, and therefore produce the backazimuthal variations observed in our results.

Second, seismic anisotropy can lead to backazimuthal variations in the scattering response. However, strong anisotropy in the mantle

Table 6. Events selected for the final 2-D-GRT inversion.

Date	Time	Lat (°N)	Lon (°E)	Depth (km)	mb	*S*	*PP*	*PS*	*SSv*	*SSh*
2006/6/18	18:28:02	33.03	−39.70	9	5.5	0	0	0	1	0
2006/6/22	10:53:11	45.42	149.34	95	6.1	1	1	0	0	0
2006/7/08	20:40:01	51.21	−179.31	22	6.2	1	1	1	0	1
2006/7/27	11:16:40	1.71	97.15	20	5.6	0	0	0	0	1
2006/7/29	19:53:43	23.59	−63.92	10	5.5	0	0	1	0	0
2006/8/20	3:01:02	49.82	156.42	26	5.8	1	1	0	0	0
2006/8/24	21:50:36	51.15	157.52	43	5.9	1	1	0	0	1
2006/9/30	17:50:23	46.35	153.17	11	6.1	1	1	0	0	1
2006/10/01	9:06:02	46.47	153.24	19	6.1	1	1	0	0	1
2006/10/09	10:01:47	20.65	120.02	14	6.0	1	1	1	1	1
2007/10/23	21:17:20	29.35	140.27	11	6.1	1	1	0	0	1
2006/11/15	11:14:14	46.59	153.27	10	6.5	1	1	0	0	0
2006/11/15	19:25:25	47.01	154.98	10	5.6	1	1	0	0	1
2006/11/15	21:22:21	47.28	154.15	12	6.0	1	1	0	0	0
2006/11/17	18:03:12	28.59	129.90	22	5.8	0	0	0	1	0
2006/12/01	3:58:21	3.39	99.08	204	6.0	1	1	0	0	0
2006/12/07	19:10:21	46.15	154.39	16	6.3	1	1	0	0	1
2006/12/09	14:48:54	47.44	147.06	396	5.6	0	0	0	0	1
2006/12/26	12:26:21	21.80	120.55	10	6.4	1	1	0	0	0
2006/12/30	8:30:50	13.31	51.37	15	5.9	0	0	1	0	1
2007/1/8	12:48:41	8.08	92.44	11	5.7	0	1	0	0	1
2007/1/15	18:17:59	34.89	138.64	170	5.7	0	1	0	0	1
2007/1/17	23:18:50	10.13	58.71	8	5.8	1	0	1	0	1
2007/2/17	0:02:56	41.79	143.55	31	5.9	0	1	0	0	1
2007/2/19	2:33:43	1.75	30.76	19	5.6	0	0	0	1	0
2007/3/06	5:49:25	−0.49	100.53	11	5.9	0	1	0	0	1
2007/3/09	3:22:42	43.22	133.53	441	6.1	1	1	0	0	0
2007/3/25	0:41:58	37.34	136.59	8	6.1	1	1	0	0	1
2007/4/03	3:35:07	36.45	70.69	222	5.7	1	1	1	1	1
2007/4/07	7:09:25	37.31	−24.49	8	5.9	0	0	0	1	0
2007/4/20	0:26:40	25.72	125.09	10	5.6	1	1	0	0	0
2007/4/29	12:41:57	52.01	−179.97	117	6.2	0	1	0	0	0
2007/5/30	20:22:12	52.14	157.29	116	6.4	1	1	0	0	1
2007/7/03	8:26:01	0.72	−30.27	10	5.8	0	0	0	1	0
2007/7/16	1:13:22	37.54	138.45	12	6.5	1	1	0	0	1
2007/7/16	14:17:37	36.81	134.85	350	6.2	1	1	0	1	1
2007/7/29	4:54:36	53.64	169.70	25	6.0	1	1	0	0	0
2007/7/30	22:42:05	19.31	95.52	14	6.0	1	1	0	0	1
2007/7/31	22:55:31	−0.16	−17.80	11	5.7	0	0	0	1	0
2007/8/08	17:04:58	−5.93	107.68	291	6.1	1	1	1	0	1
2007/8/15	20:22:11	50.32	−177.55	9	6.3	1	1	1	1	1
2007/8/20	2:56:48	−2.71	36.29	10	5.3	0	0	0	1	0
2007/8/20	22:42:28	8.04	−39.25	6	6.3	0	0	0	1	0
2007/9/13	16:09:16	−3.17	101.52	53	6.1	0	1	0	0	0
2007/9/14	6:01:32	−4.08	101.17	23	5.9	1	1	0	0	0
2007/9/19	7:27:51	−2.75	100.89	35	5.7	1	1	0	0	1
2007/9/20	8:31:14	−1.99	100.14	30	6.3	1	1	0	1	1

wedge would cause deviations between the different backscattering modes within each bin (e.g. deviations between *SSh*, *SSv* and *PP* images in bin 1), and between individual backscattering modes recorded in different bins (e.g. deviations between *SSh* images in bins 1–6). The fact that no such deviations are observed in our results suggests that anisotropy does not significantly affect the final image. Shear-wave-splitting analysis of the MEDUSA data, which will be the subject of a future study, shall provide improved constraints on seismic anisotropy in the Hellenic subduction zone.

Third, we test the possibility that the background-velocity model used in the inversion does not adequately represent material properties in the sampled volume. This situation would cause backazimuthal inconsistencies as those observed here and a general defocusing of the composite image. We recreated the images using a wide range of uniform, 1-D background-velocity models, but none of these yielded a consistent dip for the low velocity layer between *S*-mode images of different backazimuths. However, we can achieve a consistent dip when using a different background model for northern backazimuths (bins 1–4) than for other directions (bins 5–6). Relative to the base model from Table 1, which we use for bins 5–6, our preferred model for northern backazimuths entails a reduction in *S*-wave velocity of >15 per cent in the mantle and a constant *P*-wave velocity, yielding an increase in V_P/V_S from 1.76 to values ≥1.8.

The values of V_P/V_S inferred from our analysis are plausible, and could result from serpentinization of the mantle wedge or a

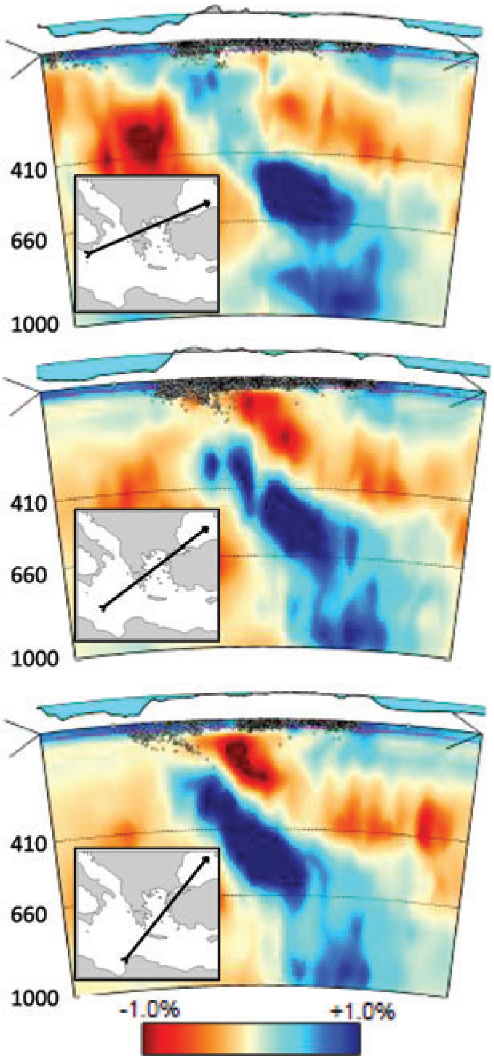

Figure 10. Profiles of *P*-wave velocity anomalies across the Hellenic subduction zone, obtained through global traveltime tomography (including traveltimes picked on data from the MEDUSA array). The three sections illustrate variations in subsurface structure along the strike of the Hellenic subduction zone. Earthquake hypocentres are indicated by black dots. The profile in the middle corresponds closely to the location and projection on which the migrated images of this study are based.

thermal anomaly. The presence of water can also reduce seismic velocities by up to 9–10 per cent depending on the assumed temperature in the mantle wedge (Karato & Eiler 2003), and therefore could play a role in the inferred high V_P/V_S ratio. We note that an elevated water content in the mantle wedge to the north of our array is somewhat inconsistent with the absence of a volcanic arc in that region, although it cannot be ruled out solely on that basis. It is also possible that rays with northern backazimuths encounter a 3-D structure of the slab (e.g. along-strike slope) that causes them to graze the slab interface—a region where elevated pore-fluid pressure causing high V_P/V_S may be encountered (see Section 7.2 and Audet *et al.* 2009). As for serpentine, theoretical calculations and seismic observations indicate that >20 per cent serpentinization can increase the V_P/V_S ratio to values of 1.8 (Hacker *et al.* 2003; Hacker & Abers 2004; Rossi *et al.* 2006). This is in agreement with a high degree of serpentinization (∼50 per cent) of the mantle wedge invoked by Sodoudi *et al.* (2006) to explain the reversed sign of Moho *P*-to-*S* conversions in the Hellenic forearc—although our model would suggest that serpentinization is more pronounced to the north of the MEDUSA array. Alternatively, the reduction in *S*-wave velocity and increase in V_P/V_S could be caused by a positive thermal anomaly of approximately 227–298 °C as inferred from experimental results (Jackson *et al.* 2002); based on the parameters suggested therein and the additional specifications: grain size $d = 1$ mm, temperature $T = 1300$–1400°C, and pressure $P = 1.0$–3.0 GPa. We note that if a slab tear should exist, it would likely reduce the grain size in that area because grain size is inversely related to shear stress (Twiss 1977; Karato *et al.* 1980; Van der Wal *et al.* 1993). In that case, a lower thermal anomaly than hypothesized above would be compatible with the presented seismic evidence.

A variation in the appropriate background model as that described above can correct the dip inconsistencies in the *S*-mode image, but it tends to overcorrect the other modes (e.g. *SSh* and *SSv*) such that they become inconsistent. This means that the simple approach we used to address this problem does not capture the full effects of deviations from the assumed background model. That is, there are probably some additional 3-D effects that are not taken into account. These observations all point to the existence of significant, along-strike, structural and/or compositional changes taking place directly to the north of the MEDUSA array. A comparison of local Wadati–Benioff seismicity with the imaged lithospheric structure (Fig. 11 and Table 2) strengthens this interpretation further. On Fig. 11 we observe that earthquakes located south of the MEDUSA array tend to cluster more within the low velocity layer than events located north of it. The images showing mismappings are created using ray paths that sample the CHSZ (Figs 2 and 1), a region that is currently undergoing great deformation (e.g. McClusky *et al.* 2000; Papanikolaou *et al.* 2007) and is underlain by a possible slab tear (Fig. 3). The slab tear could both be responsible for the 3-D perturbations that distort the seismic images, and cause an inflow of asthenospheric material into the mantle wedge (Fig. 3), which would lower *S*-wave velocities and increase the V_P/V_S ratio.

8 CONCLUSION

Our study presents high-resolution seismic images of the Hellenic subduction zone in the intermediate depth range, down to 150 km depth. Thereby, it fills an important gap in our knowledge of the Hellenic subduction zone, since many previous imaging endeavours focused on either the shallow (0–30 km) or deep (>200 km) portions of the system. The main feature detected in our images is a low-velocity layer of relatively constant thickness (15–22 km) and dip ∼21°. We interpret this layer as the oceanic crust being subducted together with a layer of sediments and perhaps an overlying layer of serpentinized mantle. The low-velocity signature of this layer persists to a depth of at least 90 km, indicating that the bulk of fluid transfer from the slab into the mantle wedge (not counting the possible serpentinite layer) occurs below this depth. In agreement with previous studies, we find that the depth of the continental Moho varies significantly below central Greece, ranging from 30 km beneath the western margin of the Aegean and the eastern Gulf of Corinth, to 40 km beneath the Hellenides. To the west of the Hellenides, beneath the western Peloponnesus, the continental Moho is not well defined. However, a pronounced discontinuity imaged at ∼20 km depth in that region probably represents the contact between low-velocity sediments and high-velocity crystalline basement.

A thorough comparison of single-mode images from distinct backazimuthal bins reveals deviations in the geometry of the

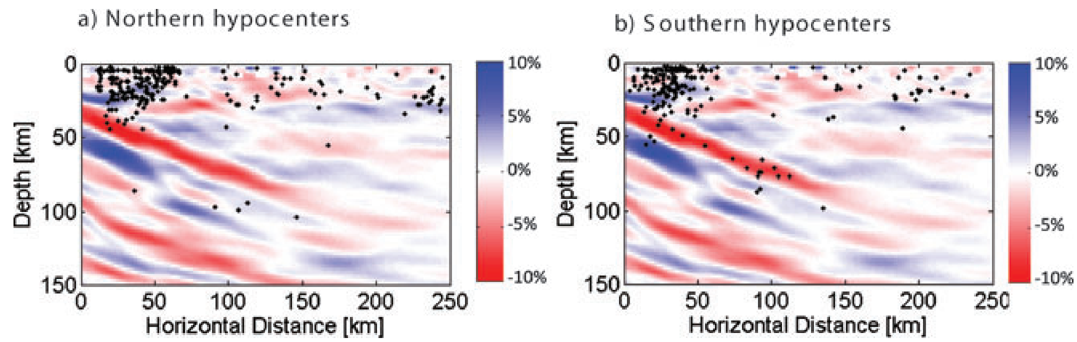

Figure 11. Comparison between the profiles obtained in this study and the local seismicity from the earthquake catalogue of the National Observatory of Athens (NOA). We plot a total of 443 hypocentres out of which 253 are located north (a) and 190 to the south (b) of the MEDUSA seismic array. These represent all events with local magnitude $M_L > 3.0$ that have occurred between 2002 June, since when the velocity model summarized in Table 2 is in use, and 2008 April 1, within 25 km epicentral distance on either side of the projection line plotted in Fig. 1. The hypocentres are plotted on top of the composite *P*-wave image similar to the one shown in Fig. 5, but recomputed using the NOA-velocity model on which the localization of the hypocentres is based (Table 2). We stress that caution is advised in comparing local hypocentres and imaged structure directly, because of the limited accuracy of hypocentre locations, but it is still interesting to note that southern hypocentres tend to cluster more in the low-velocity layer representing the subducting crust than northern ones.

subducted slab. These deviations are attributed to the existence of significant, along-strike, structural and/or compositional changes taking place directly to the north of the MEDUSA array. Although the idea of a slab detachment in the region is not new (Spakman *et al.* 1988; Carminati *et al.* 1998; Wortel & Spakman 2000), our analysis places new constraints on the location and nature of the slab deformation. It suggests that the mantle wedge below the CHSZ contains 3-D structure, and that it exhibits reduced *S*-wave velocities and increased V_P/V_S ratio relative to the mantle wedge beneath the Peloponnesus. These results provide support to the hypothesis of a slab tear below the CHSZ, which can explain both the occurrence of 3-D structure, and a thermally induced reduction in *S*-wave velocity due to inflow of asthenospheric material through the associated slab window. Taken alone, the results presented here do not allow a direct characterization of the mantle structure beneath the CHSZ. However, we expect that the addition of results from ongoing tomographic efforts, shear wave splitting analysis, and high-resolution imaging in northern Greece will yield improved structural constraints on the transition between different regimes of subduction north and south of the Kephalonia Transform.

ACKNOWLEDGMENTS

This study is supported by the NSF-grant Continental Dynamics EAR-0409373. We would like to thank the National Observatory of Athens for invaluable assistance in facilitating the field work. Furthermore, we thank IRIS-PASSCAL for providing us with instrumentation and specifically Eliana Arias for her untiring help during the initial installation and generous advice on data management. We also thank Chang Li for his valuable advice on the global tomography model presented in Fig. 10. Constructive comments from two anonymous reviewers helped improve the document.

REFERENCES

Armijo, R., Meyer, B., King, G.C.P., Rigo, A. & Papanastassiou, D., 1996. Quaternary evolution of the Corinth rift and its implications for the late Cenozoic evolution of the Aegean, *Geophys. J. Int,* **126**(1), 11–53.

Audet, P., Bostock, M.G., Christensen, N. & Peacock, S., 2009. Seismic evidence for overpressured subducted oceanic crust and megathrust fault sealing, *Nature,* **457**(7225), 76–78.

Beylkin, G., 1985. Imaging of discontinuities in the inverse scattering problem by inversion of a causal generalized Radon transform, *J. Math. Phys.,* **26,** 99–108.

Beylkin, G. & Burridge, R., 1990. Linearized inverse scattering problems in acoustics and elasticity, *Wave Motion,* **12**(1), 15–52.

Bohnhoff, M., Makris, J., Papanikolaou, D. & Stavrakakis, G., 2001. Crustal investigation of the Hellenic subduction zone using wide aperture seismic data, *Tectonophysics,* **343**(3-4), 239–262.

Bostock, M.G., Rondenay, S. & Shragge, J., 2001. Multiparameter two-dimensional inversion of scattered teleseismic body waves, 1. Theory for oblique incidence, *J. geophys. Res.,* **106**(B12), 30 771–30 782.

Bourova, E., Kassaras, I., Pedersen, H.A., Yanovskaya, T., Hatzfeld, D. & Kiratzi, A., 2005. Constraints on absolute S velocities beneath the Aegean Sea from surface wave analysis, *Geophys. J. Int.,* **160**(3), 1006–1019.

Brown, S.A.M. & Robertson, A.H.F., 2003. Sedimentary geology as a key to understanding the tectonic evolution of the Mesozoic–Early Tertiary Paikon Massif, Vardar suture zone, N Greece, *Sed. Geol.,* **160**(1-3), 179–212.

Calcagnile, G., D'Ingeo, F., Farrugia, P. & Panza, G.F., 1982. The lithosphere in the central-eastern Mediterranean area, *Pure appl. Geophys.,* **120**(2), 389–406.

Carminati, E., Wortel, M.J.R., Spakman, W. & Sabadini, R., 1998. The role of slab detachment processes in the opening of the western–central Mediterranean basins: some geological and geophysical evidence, *Earth planet. Sci. Lett.,* **160**(3-4), 651–665.

Christova, C., 1992. Seismicity depth pattern, seismic energy and b value depth variation in the Hellenic Wadati–Benioff zone, *Phys. Earth planet. Int.,* **72**(1-2), 38–48.

Clarke, P.J. *et al.*, 1998. Crustal strain in central Greece from repeated GPS measurements in the interval 1989–1997, *Geophys. J. Int.,* **135**(1), 195–214.

Clément, C., Hirn, A., Charvis, P., Sachpazi, M. & Marnelis, F., 2000. Seismic structure and the active Hellenic subduction in the Ionian islands, *Tectonophysics,* **329**(1-4), 141–156.

Clément, C., Sachpazi, M., Charvis, P., Graindorge, D., Laigle, M., Hirn, A. & Zafiropoulos, G., 2004. Reflection–refraction seismics in the Gulf of Corinth: hints at deep structure and control of the deep marine basin, *Tectonophysics,* **391**(1–4), 97–108.

Dewey, J. & Sengör, A., 1979. Aegean and surrounding regions: complex multiplate and continuum tectonics in a convergent zone, *Geol. Soc. Amer. Bull.,* **90**(1), 84–92.

Dueker, K. & Sheehan, A., 1997. Mantle discontinuity structure from midpoint stacks of converted P to S waves across the Yellowstone hotspot track, *J. geophys. Res,* **102**(B4), 8313–8327.

Endrun, B., Ceranna, L., Meier, T., Bohnhoff, M. & Harjes, H.P., 2005. Modeling the influence of Moho topography on receiver functions:

A case study from the central Hellenic subduction zone, *Geophys. Res. Lett.,* **32**(12), L12311.

Endrun, B., Meier, T., Lebedev, S., Bohnhoff, M., Stavrakakis, G. & Harjes, H.P., 2008. S velocity structure and radial anisotropy in the Aegean region from surface wave dispersion, *Geophys. J. Int.,* **174**(2), 593–616.

Ferris, A., Abers, G., Christensen, D. & Veenstra, E., 2003. High resolution image of the subducted Pacific (?) plate beneath central Alaska, 50–150 km depth, *Earth planet. Sci. Lett.,* **214**(3-4), 575–588.

Finetti, I., 1982. Structure, stratigraphy and evolution of the Central Mediterranean, *Boll. Geof. Teor. Appl.,* **24**(96), 247–312.

Finetti, J., Papanikolaou, D., Del Ben, A. & Karvelis, P., 1991. Preliminary geotectonic interpretation of the East Mediterranean chain and the Hellenic arc, *Bull. Geol. Soc. Greece,* **25**(1), 509–526.

Fytikas, M., Giuliani, O., Innocenti, F., Marinelli, G. & Mazzuoli, R., 1976. Geochronological data on recent magmatism of the Aegean Sea, *Tectonophysics,* **31**(1-2), 29–34.

Fytikas, M., Innocenti, F., Manetti, P., Peccerillo, A., Mazzuoli, R. & Villari, L., 1984. Tertiary to Quaternary evolution of volcanism in the Aegean region, *Geol. Soc. Lon. Spec. Publ.,* **17**(1), 687–699.

Gesret, A., Hirn, A., Sachpazi, M., Diaz, J. & Laigle, M., 2009. Fine structure at the subducting slab top under E Peloponnesus (Greece) from multiscale receiver-function approach, *under review*.

Hacker, B.R. & Abers, G.A., 2004. Subduction Factory 3. An Excel worksheet and macro for calculating the densities, seismic wave speeds, and H_2O contents of minerals and rocks at pressure and temperature, *Geochem. Geophys. Geosyst,* **5,** Q01005.

Hacker, B.R., Abers, G.A. & Peacock, S., 2003. Subduction factory: 1. Theoretical mineralogy, densities, seismic wave speeds, and H_2O contents, *J. geophys. Res,* **108**(B1), 2029.

Hearn, T., 1999. Uppermost mantle velocities and anisotropy beneath Europe, *J. geophys. Res.,* **104**(B7), 15 123–15 139.

Hirn, A., Sachpazi, M., Siliqi, R., Mc Bride, J., Marnelis, F., Cernobori, L. & the STREAMERS-PROFILES group, 1996. A traverse of the Ionian islands front with coincident normal incidence and wide-angle seismics, *Tectonophysics,* **264**(1-4), 35–49.

Hosa, A., 2008. Imaging of the Hellenic subduction zone by seismic tomography, *BS thesis*, M.I.T., Cambridge, MA, USA.

Jackson, I., Fitz Gerald, J., Faul, U. & Tan, B., 2002. Grain-size-sensitive seismic wave attenuation in polycrystalline olivine, *J. geophys. Res,* **107**(B12), 2360.

Jacobshagen, V., Durr, S., Kockel, F., Kopp, K. & Kowalezyyk, G., 1978. Structure and geodynamic evolution of the Aegean region, in *Alps, Apennines, Hellenides,* pp. 538–564, eds Cloos, H., Roeder, D. & Schmidt, K., E. Schweizbart'sche Verlagsbuchhandlung.

Kahle, H.G., Müller, M.V., Mueller, S. & Veis, G., 1993. The Kephalonia Transform fault and the rotation of the Apulian platform: evidence from satellite geodesy, *Geophys. Res. Lett.,* **20**(8), 651–654.

Karagianni, E.E., Papazachos, C.B., Panagiotopoulos, D.G., Suhadolc, P., Vuan, A. & Panza, G., 2005. Shear velocity structure in the Aegean area obtained by inversion of Rayleigh waves, *Geophys. J. Int.,* **160**(1), 127–143.

Karason, H., 2002. Constraints on mantle convection from seismic tomography and flow modeling, *PhD thesis*, Massachusetts Institute of Technology.

Karato, S.I. & Eiler, J., 2003. Mapping Water content in the upper mantle, in *Inside the Subduction Factory,* pp. 135–152, ed Eiler, J., AGU Monograph.

Karato, S., Toriumi, M. & Fujii, T., 1980. Dynamic recrystallization of olivine single crystals during high-temperature creep, *Geophys. Res. Lett,* **7**(9), 649–652.

Kawakatsu, H. & Watada, S., 2007. Seismic evidence for deep-water transportation in the mantle, *Science,* **316**(5830), 1468–1471.

Knapmeyer, M. & Harjes, H., 2000. Imaging crustal discontinuities and the downgoing slab beneath western Crete, *Geophys. J. Int.,* **143**(1), 1–21.

Kokinou, E., Kamberis, E., Vafidis, A., Monopolis, D., Ananiadis, G. & Zelilidis, A., 2005. Deep seismic reflection data from offshore western Greece: a new crustal model for the Ionian sea, *J. Petr. Geol.,* **28**(2), 185–202.

Kokinou, E., Vafidis, A., Loucogiannakis, M. & Louis, I., 2003. Deep seismic imaging and velocity estimation in Ionian Sea, *J. Balkan Geophys. Soc.,* **6**(2), 100–116.

Kopf, A., Mascle, J. & Klaeschen, D., 2003. The Mediterranean Ridge: a mass balance across the fastest growing accretionary complex on Earth, *J. geophys. Res.,* **108**(B8), 2372.

Kreemer, C., Chamot-Rooke, N. & Le Pichon, X., 2004. Constraints on the evolution and vertical coherency of deformation in the Northern Aegean from a comparison of geodetic, geologic and seismologic data, *Earth planet. Sci. Lett.,* **225**(3-4), 329–346.

Le Pichon, X. & Angelier, J., 1979. The Hellenic arc and trench system: A key to the neotectonic evolution of the eastern Mediterranean area, *Tectonophysics,* **60,** 1–42.

Le Pichon, X. & Angelier, J., 1981. The Aegean Sea, *Phil. Trans. R. Soc. Lond., Series A,* **300**(1454), 357–372.

Li, X. *et al.*, 2003. Receiver function study of the Hellenic subduction zone: imaging crustal thickness variations and the oceanic Moho of the descending African lithosphere, *Geophys. J. Int.,* **155**(2), 733–748.

Ligdas, C.N., Main, I.G. & Adams, R.D., 1990. 3-D structure of the lithosphere in the Aegean region, *Geophys. J. Int,* **102**(1), 219–229.

Di Luccio, F. & Pasyanos, M.E., 2007. Crustal and upper-mantle structure in the Eastern Mediterranean from the analysis of surface wave dispersion curves, *Geophys. J. Int.,* **169**(3), 1139–1152.

Makris, J., 1978. The crust and upper mantle of the Aegean region from deep seismic soundings, *Tectonophysics,* **46**(3-4), 269–284.

Marone, F., van der Meijde, M., van der Lee, S. & Giardini, D., 2003. Joint inversion of local, regional and teleseismic data for crustal thickness in the Eurasia-Africa plate boundary region, *Geophys. J. Int.,* **154**(2), 499–514.

Martínez, M.D., Canas, J.A., Lana, X. & Badal, J., 2001. Objective regionalization of Rayleigh wave dispersion data by clustering algorithms: an application to the Mediterranean basin, *Tectonophysics,* **330**(3-4), 245–266.

Martinod, J. & Davy, P., 1992. Periodic instabilities during compression or extension of the lithosphere 1. Deformation modes from an analytical perturbation method, *J. geophys. Res,* **97**(B2), 1999–2014.

Mascle, J. & Chaumillon, E., 1998. An overview of Mediterranean Ridge collisional accretionary complex as deduced from multichannel seismic data, *Geo-Marine Lett.,* **18**(2), 81–89.

McClusky, S. *et al.*, 2000. Global Positioning System constraints on plate kinematics and dynamics in the eastern Mediterranean and Caucasus, *J. geophys. Res.,* **105**(B3), 5695–5719.

McKenzie, D., 1970. Plate tectonics of the Mediterranean region, *Nature,* **226**(5242), 239–243.

McKenzie, D., 1972. Active tectonics of the Mediterranean region, *Geophys. J. R. astr. Soc.,* **30**(2), 109–185.

McKenzie, D., 1978. Active tectonics of the Alpine-Himalayan belt: the Aegean Sea and surrounding regions, *Geophys. J. R. astr. Soc,* **55**(1), 217–254.

McNamara, D.E. & Boaz, R., 2005. Seismic Noise Analysis System, Power Spectral Density Probability Density Function: Stand-Alone Software Package, Tech. rep., USGS Open-File Report.

McNamara, D.E. & Buland, R.P., 2004. Ambient Noise Levels in the Continental United States, *Bull. seism. Soc. Am.,* **94**(4), 1517–1527.

Meier, T., Rische, M., Endrun, B., Vafidis, A. & Harjes, H.P., 2004. Seismicity of the Hellenic subduction zone in the area of western and central Crete observed by temporary local seismic networks, *Tectonophysics,* **383**(3-4), 149–169.

Miller, D., Oristaglio, M. & Beylkin, G., 1987. A new slant on seismic imaging: migration and integral geometry, *Geophysics,* **52**(7), 943–964.

Neumann, P. & Zacher, W., 2004. The Cretaceous sedimentary history of the Pindos Basin (Greece), *Int. J. Earth Sci.,* **93**(1), 119–131.

Papanikolaou, D., 1993. Geotectonic evolution of the Aegean, *Bull. Geol. Soc. Greece,* **27,** 33–48, eds Cavazzu, W., Roure F., Spaman W., Stampfli G.M., Ziegler P.A., Publication of the Mediterranean Consertium for the 32nd International Geological Congress. Springer Berlin Heidelberg.

Papanikolaou, D. *et al.*, 2004. Transect VII: east European Craton–Scythian Platform–Dobrogea–Balkanides–Rhodope Massif–Hellenides–East Mediterranean–Cyrenaica, in *The TRANSMED Atlas. The*

Mediterranean Region from Crust to Mantle, Geological and Geophysical Framework., Springer.

Papanikolaou, D., Fountoulis, I. & Metaxas, C., 2007. Active faults, deformation rates and Quaternary paleogeography at Kyparissiakos Gulf (SW Greece) deduced from onshore and offshore data, *Quat. Int.*, **171,** 14–30.

Papazachos, C. & Nolet, G., 1997. P and S deep velocity structure of the Hellenic area obtained by robust nonlinear inversion of travel times, *J. geophys. Res.*, **102**(B4), 8349–8367.

Papazachos, B.C., Karakostas, V.E., Papazachos, C.B. & Scordilis, E.M., 2000. The geometry of the Wadati–Benioff zone and lithospheric kinematics in the Hellenic arc, *Tectonophysics,* **319**(4), 275–300.

Pasyanos, M.E. & Walter, W.R., 2002. Crust and upper-mantle structure of North Africa, Europe and the Middle East from inversion of surface waves, *Geophys. J. Int.*, **149**(2), 463–481.

Peter, Y., Kahle, H., Cocard, M., Veis, G., Felekis, S. & Paradissis, D., 1998. Establishment of a continuous GPS network across the Kephalonia Fault Zone, Ionian islands, Greece, *Tectonophysics,* **294**(3-4), 253–260.

Peterson, J., 1993. Observation and modeling of seismic background noise, 93-322, U.S. Geol. Surv. Tech. Rept.

Piromallo, C. & Morelli, A., 2003. P wave tomography of the mantle under the Alpine-Mediterranean area, *J. geophys. Res.*, **108**(B2), 2065.

Rondenay, S., Bostock, M.G. & Shragge, J., 2001. Multiparameter two-dimensional inversion of scattered teleseismic body waves, 3. Application to the Cascadia 1993 data set, *J. geophys. Res.*, **106**(12), 30 795–30 807.

Rondenay, S., Bostock, M.G. & Fischer, K., 2005. Multichannel inversion of scattered teleseismic body waves: practical considerations and applicability, in *Seismic Earth: Array Analysis of Broadband Seismograms,* Vol. 157, eds Levander, A. & Nolet, G., AGU Geophysical Monograph Series, 187–204.

Rondenay, S., Abers, G.A. & van Keken, P., 2008. Seismic imaging of subduction zone metamorphism, *Geology,* **36**(4), 275–278.

Rossi, G., Abers, G.A., Rondenay, S. & Christensen, D.H., 2006. Unusual mantle Poisson's ratio, subduction, and crustal structure in central Alaska, *J. geophys. Res.*, **111**(B9), B09311.

Royden, L., 1993. The tectonic expression of slab pull at continental convergent boundaries, *Tectonics,* **12**(2), 303–325.

Rüpke, L.H., Morgan, J.P., Hort, M. & Connolly, J.A.D., 2004. Serpentine and the subduction zone water cycle, *Earth planet. Sci. Lett.*, **223**(1-2), 17–34.

Sachpazi, M. *et al.*, 2007. Moho topography under central Greece and its compensation by Pn time-terms for the accurate location of hypocenters: the example of the Gulf of Corinth 1995 Aigion earthquake, *Tectonophysics,* **440**(1-4), 53–65.

Saunders, P., Priestley, K. & Taymaz, T., 1998. Variations in the crustal structure beneath western Turkey, *Geophys. J. Int.*, **134**(2), 373–389.

Schmid, C., van der Lee, S. & Giardini, D., 2004. Delay times and shear wave splitting in the Mediterranean region, *Geophys. J. Int.*, **159**(1), 275–290.

Schmid, C., van der Lee, S. & Giardini, D., 2006. Correlated shear and bulk moduli to 1400 km beneath the Mediterranean region, *Phys. Earth planet. Int.*, **159**(3-4), 213–224.

Schurr, B., Asch, G., Rietbrock, A., Trumbull, R. & Haberland, C., 2003. Complex patterns of fluid and melt transport in the central Andean subduction zone revealed by attenuation tomography, *Earth planet. Sci. Lett.*, **215**(1-2), 105–119.

Shragge, J., Bostock, M.G. & Rondenay, S., 2001. Multiparameter two-dimensional inversion of scattered teleseismic body waves: 2. Numerical examples, *J. geophys. Res,* **106**(12), 30 783–30 793.

Snopek, K., Meier, T., Endrun, B., Bohnhoff, M. & Casten, U., 2007. Comparison of gravimetric and seismic constraints on the structure of the Aegean lithosphere in the forearc of the Hellenic subduction zone in the area of Crete, *J. Geodyn.*, **44**(3–5), 173–185.

Sodoudi, F. *et al.*, 2006. Lithospheric structure of the Aegean obtained from P and S receiver functions, *J. geophys. Res.*, **111**(B12), B12307.

Spakman, W., Wortel, M.J.R. & Vlaar, N.J., 1988. The Hellenic subduction zone: a tomographic image and its geodynamic implications, *Geophys. Res. Lett.*, **15**(1), 60–63.

Spakman, W., van der Lee, S. & van der Hilst, R.D., 1993. Travel-time tomography of the European-Mediterranean mantle down to 1400 km, *Phys. Earth planet. Int.*, **79**(1-2), 3–74.

Tiberi, C. *et al.*, 2000. Crustal and upper mantle structure beneath the Corinth rift (Greece) from a teleseismic tomography study, *J. geophys. Res.*, **105**(B12), 28 159–28 171.

Tiberi, C., Diament, M., Lyon-Caen, H. & King, T., 2001. Moho topography beneath the Corinth Rift area (Greece) from inversion of gravity data, *Geophys. J. Int.*, **145**(3), 797–808.

Tirel, C., Gueydan, F., Tiberi, C. & Brun, J.P., 2004. Aegean crustal thickness inferred from gravity inversion. Geodynamical implications, *Earth planet. Sci. Lett.*, **228**(3-4), 267–280.

Tsokas, G.N. & Hansen, R.O., 1997. Study of the crustal thickness and the subducting lithosphere in Greece from gravity data, *J. geophys. Res.*, **102**(B9), 20 585–20 597.

Twiss, R.J., 1977. Theory and applicability of a recrystallized grain size paleopiezometer, *Pure appl. Geophys.*, **115**(1), 227–244.

van der Hilst, R.D., Widiyantoro, S. & Engdahl, E.R., 1997. Evidence for deep mantle circulation from global tomography, *Nature,* **386**(6625), 578–584.

van der Meijde, M., van der Lee, S. & Giardini, D., 2003. Crustal structure beneath broad-band seismic stations in the Mediterranean region, *Geophys. J. Int.*, **152**(3), 729–739.

Van der Wal, D., Chopra, P., Drury, M. & Fitz Gerald, J.D., 1993. Relationships between dynamically recrystallized grain size and deformation conditions in experimentally deformed olivine rocks, *Geophys. Res. Lett.*, **20**(14), 1479–1482.

Wortel, M.J.R. & Spakman, W., 2000. Subduction and slab detachment in the Mediterranean-Carpathian Region, *Science,* **290**(5498), 1910–1917.

Zelt, B.C., Taylor, B., Sachpazi, M. & Hirn, A., 2005. Crustal velocity and Moho structure beneath the Gulf of Corinth, Greece, *Geophys. J. Int.*, **162**(1), 257–268.

Zhang, H.J., Thurber, C.H., Shelly, D., Ide, S., Beroza, G.C. & Hasegawa, A., 2004. High-resolution subducting-slab structure beneath northern Honshu, Japan, revealed by double-difference tomography, *Geology,* **32**(4), 361–364.

Zhu, L.P., Mitchell, B.J., Akyol, N., Cemen, I. & Kekovali, K., 2006. Crustal thickness variations in the Aegean region and implications for the extension of continental crust, *J. geophys. Res,* **111**(B1), B0130.

SUPPORTING INFORMATION

Additional Supporting Information may be found in the online version of this article:

Appendix S1. The supplement reports on noise analysis, receiver functions, and additional results from the 2-D-GRT inversion of data from the temporary MEDUSA seismic array that are complementary to the material discussed in the paper.

Please note: Wiley-Blackwell are not responsible for the content or functionality of any supporting material supplied by the authors. Any queries (other than missing material) should be directed to the corresponding author for the article.